

Delft University of Technology
Faculty of Mechanical, Maritime and Materials Engineering;
Department of Biomedical Engineering
Leiden University Medical Center
C.J. Gorter MRI Center

Dynamic B_0 Inhomogeneity Correction at Low Field (50mT) using Interleaved B_0 Mapping

Applied to Turbo Spin Echo and Magnetic
Resonance Fingerprinting
Master thesis

H.E. Nijse

Student nr.: 4574966

MSc Biomedical Engineering, Track: Medical Physics
Delft, the Netherlands

April 7th, 2022

Supervisors:

Dr. ir. K. Koolstra - LUMC

Dr. F.M. Vos - TU Delft



Abstract

Low-field MRI is susceptible to temperature changes in magnet temperature, resulting in time-dependent inhomogeneities. This causes time-dependent phase shifts in the measured signal, leading to image distortions. In this project, a method is proposed to interleave short magnetic field (B_0) mapping sequences in the target image acquisition for Turbo Spin Echo (TSE) and Magnetic Resonance Fingerprinting (MRF). Simulations show that the proposed correction method works in 2D. Experiment results show that interleaved B_0 mapping can be done at relatively low spatial and temporal resolution, shortening the B_0 acquisition time. Also, the distortion correction works for both TSE and MRF, though its advantages over static inhomogeneity correction are limited to acquisitions with a small bandwidth per voxel and large or very inhomogeneous frequency drifts.

List of abbreviations

MRI - Magnetic Resonance Imaging
TSE - Turbo Spin Echo
MRF - Magnetic Resonance Fingerprinting
GE - Gradient Echo
SE - Spin Echo
ETL - Echo Train Length
FA - Flip Angle
FOV - Field of view
MC - Matrix Completion
CPR - Conjugate Phase Reconstruction
SSFP - Steady State Free Precession
FISP - Fast Imaging with Steady State Free Precession
SH - Spherical Harmonics

Contents

1	Introduction	1
2	Theoretical background	2
2.1	Temperature effects	2
2.2	Signal equations for inhomogeneous B_0 , 3D	2
2.2.1	Signal without B_0	2
2.2.2	B_0 influence on k-space signal	2
2.2.3	Sanity check: spatially and temporally constant B_0	3
2.3	B_0 correction	3
2.4	B_0 mapping	4
2.4.1	B_0 mapping methods for Spin Echo sequences	4
2.4.2	B_0 mapping methods for Gradient Echo sequences	4
2.5	MRI Sequences: TSE and MRF	5
2.5.1	Turbo Spin Echo	5
2.5.2	Magnetic Resonance Fingerprinting	5
3	Methodology	8
3.1	MRF Simulations	8
3.1.1	Phantom design	8
3.2	Interleaved B_0 mapping	9
3.2.1	Interleaved B_0 mapping for TSE imaging	9
3.2.2	Interleaved B_0 mapping for fingerprinting	9
3.2.3	B_0 map acquisition parameter optimisation in TSE	11
3.3	Image correction	11
3.3.1	Image correction pipeline for TSE	11
3.3.2	Image correction pipeline for MRF	12
3.4	Experimental setup	12
3.4.1	Phantoms	12
3.4.2	Measurements	13
3.4.3	Hardware	13
4	Results	15
4.1	MRF Simulation	15
4.2	Optimizing B_0 mapping parameters	19
4.3	Distortion correction in TSE	19
4.4	Distortion correction in MRF	24
5	Discussion	28
5.1	Simulation	28
5.2	Optimizing B_0 mapping parameters	28
5.3	Distortion correction in TSE	29
5.4	Distortion correction in MRF	29
5.5	Minimizing additional scan time	30
6	Conclusion	31
7	Acknowledgements	32

1 Introduction

Over the years, many technological developments have improved magnetic resonance imaging (MRI). More reliable hardware, faster algorithms and a better understanding of the underlying physics have made MRI an increasingly powerful tool for medical research and diagnostics.

However, the complexity of the technology leads to high installation and maintenance costs. Rather than making the technology more accessible by decreasing the costs, modern improvements to hardware and software have only made the technology more expensive. This is reflected in the availability of MR scanners worldwide and even within western countries [1], [2]. Especially citizens of developing countries have little to no access to MR technology [3].

This unequal distribution of healthcare has increased the interest in low-field, permanent magnet MRI. Using this technology, the complexity of the system decreases and requirements on hardware and amplifiers are lower, thus reducing costs [3], [4]. Besides, a lower field strength leads to increased patient safety [3]. Such a system has the potential to become portable, thus accommodating point-of-care healthcare. These advantages come at the cost of image quality however. Still, a concrete application remains diagnosis and treatment for infant hydrocephalus [5], which occurs relatively often in the developing world compared to the western world.

For the last years, the Low Field Group of the Leiden University Medical Center (LUMC) has been developing such a scanner, a 50mT permanent magnet system. This scanner is a low-cost, light-weight, portable MR system which is capable of acquiring human (in-vivo) images at reasonable acquisition times. This low-field system has challenges as well, as the static and dynamic magnetic field (B_0) inhomogeneities are stronger, in the order of 2400 ppm [4]. This leads to image distortions, although correction methods have already been applied successfully [6].

Additionally, the scanner is susceptible to temperature changes, as an increase in temperature lowers the strength of the permanent magnets [7]. When the scanner heats up during acquisition, for example due to heat radiating from the patient, B_0 will become time-dependent. Research has shown that the B_0 drift can be in the order of 800 Hz/hour [4] or 4kHz per degree Celsius [8]. Depending on the bandwidth per voxel and the length of the sequence, this can lead to a time-dependent signal shift of several voxels.

In general long, and especially gradient-echo based sequences are susceptible to this B_0 drift. The resulting image distortions may also affect quantitative values derived from these images, such as done in Magnetic Resonance Fingerprinting (MRF).

The purpose of this master thesis research project is to monitor and correct for dynamic changes in B_0 . A method is proposed to track inhomogeneity and drift over time. This B_0 mapping sequence, and the correction, has been implemented and tested on a Turbo Spin Echo (TSE) sequence. A similar approach has been used to correct MRF data. Furthermore, the effect of B_0 inhomogeneities and drift is studied on the quantitative parameter maps of the MRF sequence in simulations and in phantom scans.

This thesis is part of a graduation project of the master Biomedical Engineering, track Medical Physics of Delft University of Technology (TU Delft) in Delft, in collaboration with the C.J. Gorter MRI Center of the Leiden University Medical Center (LUMC) in Leiden.

2 Theoretical background

This section describes relevant background information on several topics related to MR and MR imaging sequences. It starts with an explanation of temperature effects, followed by a mathematical exposition of how resulting B_0 inhomogeneities influence the k-space data. A description of methods to measure B_0 is given, and both Turbo Spin Echo (TSE) and Magnetic Resonance Fingerprinting (MRF) are discussed.

2.1 Temperature effects

The field inside the 50mT system is created by a permanent array of magnets in a discretized version of a Halbach magnet [4], whereas clinical higher-field systems generally use a superconducting magnet cooled by liquid helium in a cryostat. This means that whereas the field of a superconducting magnet can be considered static because of the carefully controlled environment, the small magnets in the Halbach array are subject to changing conditions in the examination room.

One of the most important factors is the magnet temperature. During a normal imaging procedure, the scanner room will heat up due to body heat, which will influence the magnet temperature. Additionally, heating of the nearby gradient coils will result in an increased temperature. When the magnet heats, the spins start to lose their alignment, thus resulting in a lower magnetic field [7].

This temperature-induced drift is about 800 Hz/hour in the current setup [4], which, depending on acquisition parameters, may lead to a shift of several voxels. The heating is not likely to be homogeneous, as some of the magnets constituting the low-field magnet are closer to the heat source than others. Also, the magnet does not react instantaneously to temperature changes. Therefore the resulting B_0 is not expected to be homogeneous nor static either, especially when imaging outside carefully controlled laboratory conditions.

2.2 Signal equations for inhomogeneous B_0 , 3D

2.2.1 Signal without B_0

In MR imaging, the measured signal \mathbf{S} is related to the image $\mathbf{m}(\mathbf{r})$ by a Fourier transformation as follows [9]:

$$S(\mathbf{k}(t)) = \int \mathbf{m}(\mathbf{r}) e^{-i2\pi\mathbf{k}(t)\cdot\mathbf{r}} d^3\mathbf{r} \quad (1)$$

where $\mathbf{k}(t)$ is the vector containing the k-space coordinates. These are computed via the relation between k-space and the applied gradients: $k(t) = \frac{\gamma}{2\pi} \int_0^t G(t') dt'$, with γ the gyromagnetic ratio, $2.675 \cdot 10^8$ rad/s/T [9]. In practice, equation 1 is discretized:

$$S(\mathbf{k}(t)) = \sum_{n=0}^{N-1} \mathbf{m}(\mathbf{r}_n) e^{-i2\pi\mathbf{k}(t)\cdot\mathbf{r}_n} \Delta r \quad (2)$$

with N the number of image pixels and a scaling factor $\Delta r = \Delta x \Delta y \Delta z$.

2.2.2 B_0 influence on k-space signal

The presence of a B_0 -offset (homogeneous or inhomogeneous) ΔB_0 introduces a phase shift, which can be written as an additional exponential factor in the equation. ΔB_0 has the unit of Tesla (T), but is often expressed in Hertz (Hz): ΔB_0 [Hz] = $\frac{\gamma}{2\pi}$ [Hz/T] $\cdot \Delta B_0$ [T]. This convention will be followed in this report, unless explicitly stated otherwise.

The magnitude of the phase shift depends on the spatially and time-dependent ΔB_0 -field in pixel n , $\Delta B_0(\mathbf{r}_n, t)$, and the total time the spins experience the field. Thus the corrupted k-space as function

of \mathbf{k} and time, $Y(\mathbf{k}(t), t)$ is given by the discretized version of [10]:

$$Y(\mathbf{k}(t), t) = \sum_{n=1}^N \mathbf{m}(\mathbf{r}_n) e^{-i2\pi\mathbf{k}(t)\cdot\mathbf{r}_n} e^{-i2\pi\Delta B_0(\mathbf{r}_n, t)t} \quad (3)$$

This discretization can be extended for different measurement times t_i , representing different readout lines, and written as a matrix multiplication:

$$\begin{bmatrix} Y(\mathbf{k}(t_1), t_1) \\ \dots \\ Y(\mathbf{k}(t_m), t_m) \end{bmatrix} = \begin{bmatrix} e^{-i2\pi\mathbf{k}(t_1)\cdot\mathbf{r}_1} e^{-i2\pi\Delta B_0(\mathbf{r}_1)t_1} & \dots & e^{-i2\pi\mathbf{k}(t_1)\cdot\mathbf{r}_N} e^{-i2\pi\Delta B_0(\mathbf{r}_N)t_1} \\ \dots & \dots & \dots \\ e^{-i2\pi\mathbf{k}(t_m)\cdot\mathbf{r}_1} e^{-i2\pi\Delta B_0(\mathbf{r}_1)t_m} & \dots & e^{-i2\pi\mathbf{k}(t_m)\cdot\mathbf{r}_N} e^{-i2\pi\Delta B_0(\mathbf{r}_N)t_m} \end{bmatrix} \begin{bmatrix} \mathbf{m}(r_1) \\ \dots \\ \mathbf{m}(r_N) \end{bmatrix} \quad (4)$$

For convenience, this can be rewritten to

$$\mathbf{Y} = \mathbf{E}(\Delta B_0)\mathbf{m} \quad (5)$$

where $\mathbf{E}(\Delta B_0)$ is the matrix containing both k-space coordinates and exponential factors.

2.2.3 Sanity check: spatially and temporally constant B_0

In the case of a constant and homogeneous ΔB_0 , Equation 4 should reduce to a constant phase shift for every $Y(\mathbf{k}(t_i), t_i)$. This is easily checked by replacing $\Delta B_0(\mathbf{r}_i, t_i)$ by ΔB_0 , leading to:

$$\begin{bmatrix} Y(\mathbf{k}(t_1), t_1) \\ \dots \\ Y(\mathbf{k}(t_m), t_m) \end{bmatrix} = \begin{bmatrix} e^{-i2\pi\Delta B_0 t_1} & & 0 \\ & \ddots & \\ 0 & & e^{-i2\pi\Delta B_0 t_m} \end{bmatrix} \begin{bmatrix} e^{-i2\pi\mathbf{k}(t_1)\cdot\mathbf{r}_1} & \dots & e^{-i2\pi\mathbf{k}(t_1)\cdot\mathbf{r}_N} \\ \dots & \dots & \dots \\ e^{-i2\pi\mathbf{k}(t_m)\cdot\mathbf{r}_1} & \dots & e^{-i2\pi\mathbf{k}(t_m)\cdot\mathbf{r}_N} \end{bmatrix} \begin{bmatrix} \mathbf{m}(r_1) \\ \dots \\ \mathbf{m}(r_N) \end{bmatrix}$$

which reduces to

$$\begin{bmatrix} Y(\mathbf{k}(t_1), t_1) \\ \dots \\ Y(\mathbf{k}(t_m), t_m) \end{bmatrix} = \begin{bmatrix} e^{-i2\pi\Delta B_0 t_1} S(\mathbf{k}(t_1), t_1) \\ \dots \\ e^{-i2\pi\Delta B_0 t_m} S(\mathbf{k}(t_m), t_m) \end{bmatrix}$$

which indeed describes a constant phase shift for each k-space point.

2.3 B_0 correction

The image \mathbf{m} in Equation 5 can be recovered from the corrupted k-space data \mathbf{Y} by taking the (pseudo)inverse of matrix \mathbf{E} , \mathbf{E}^\dagger , and using an estimated ΔB_0 , leading to:

$$\mathbf{m} = \mathbf{E}(\Delta B_0)^\dagger \mathbf{Y} \quad (6)$$

Due to the size of \mathbf{E} however, the computation of the pseudo-inverse in this model-based method will take very long. An alternative would be using linear solvers, such as the conjugate gradient method (CG) [11]. The non-linear Split Bregman scheme has been applied successfully in distortion correction [6], although it may be relatively slow.

Alternatively, there are mathematical models that reduce reconstruction times, like conjugate phase reconstruction (CPR) [6], [12]. This method approximates the inverse of Equation 3 as

$$m(\mathbf{r}) \approx \sum_{n=1}^{N_t} \mathbf{Y}(\mathbf{k}(t_n)) e^{i2\pi\mathbf{k}(t_n)\cdot\mathbf{r}} e^{i2\pi\Delta B_0(\mathbf{r}, t_n)t_n} \Delta t \quad (7)$$

where also the magnetic field ΔB_0 is time-dependent.

2.4 B₀ mapping

In order to use the CPR method described above to correct for dynamic B₀ changes, the time-dependent B₀ map should be monitored during the acquisition of the image. This can be done in many different ways.

In an earlier project some possibilities were explored to monitor B₀ by adding frequency probes to the imaging coil [13]. These probes, placed strategically around the coil, measure the resonance frequency, which is related to the B₀ field. An advantage of this method is that it is fast and reasonably accurate at the location of the measurement, eliminating mistakes or inaccuracies introduced by the scanning protocol. However, as the probes are placed around the imaging coil, only the field outside the phantom or patient is known. Thus, they do not directly assess the field inside the phantom or patient, and this method relies on interpolation by spherical harmonics (SH) fitting for the results.

Another way to monitor B₀ is by using B₀ mapping sequences. This can either be by adding a B₀ pre-scan, or by estimating B₀ from the images in the acquisition sequence. At the expense of introducing additional scan time, the maps that are acquired show the B₀ distribution within the object and may therefore be more reliable.

2.4.1 B₀ mapping methods for Spin Echo sequences

In Spin Echo (SE)-based sequences, like Turbo Spin Echo (TSE), there is complete rephasing of the spins at the center of the echo. This includes the rephasing of additional dephasing due to field inhomogeneities.

A method currently used to map the ΔB₀ inhomogeneities in SE-based sequences, is by using a shift of the readout gradient [6]. When the readout is shifted with a time t_{shift} , such that the center of the readout is not at the center of the actual spin echo anymore, a phase factor is introduced in the signal.

The phase factor for the unshifted readout, $\phi_{unshifted}(\mathbf{r})$, can be written as

$$e^{-i\phi_{unshifted}(\mathbf{r})} = e^{-2\pi\Delta B_0(\mathbf{r})it+C(r)}$$

for $t = 0$ at the center of the readout. $C(r)$ stands for the phase caused by other sources, like receiver phase. The phase factor, $\phi_{shifted}(\mathbf{r})$, for the shifted readout can be written as:

$$e^{-i\phi_{shifted}(\mathbf{r})} = e^{-2\pi\Delta B_0(\mathbf{r})i(t+t_{shift})+C(r)}$$

Defining the phase map due to inhomogeneities as

$$\Delta\phi(\mathbf{r}) = \phi_{shifted}(\mathbf{r}) - \phi_{unshifted}(\mathbf{r})$$

this can be rewritten as

$$\Delta\phi(\mathbf{r}) = 2\pi\Delta B_0(\mathbf{r})t_{shift}$$

from which it follows that

$$\Delta B_0(\mathbf{r}) = \frac{\Delta\phi(\mathbf{r})}{2\pi t_{shift}} \quad (8)$$

Thus, the phase effects caused by other sources will cancel out between shifted and unshifted acquisitions, leaving the phase effects caused by B₀ inhomogeneities.

2.4.2 B₀ mapping methods for Gradient Echo sequences

For Gradient Echo (GE)-based sequences, like magnetic resonance fingerprinting (MRF), the amount of phase distortion due to inhomogeneities in the ΔB₀ field depends on the selected echo time, TE. The rephasing with the gradient only works for the dephasing caused by the gradient, and does not compensate for B₀-induced dephasing. Therefore, every image will contain some degree of phase

distortions due to ΔB_0 . The ΔB_0 -phase effect will mostly depend on the echo time TE, as this determines how long the spins have experienced a different magnetic field. The length of the readout also influences the phase distortions, although the effect of this is usually smaller than the TE-effect. By comparing two images with different echo times therefore, the magnetic field can be estimated.

Consider image 1 with echo time TE_1 , and image 2 with echo time TE_2 . The B_0 -related phase accumulations are given by:

$$e^{-i\phi_1} = e^{-2\pi\Delta B_0(\mathbf{r})iTE_1}, e^{-i\phi_2} = e^{-2\pi\Delta B_0(\mathbf{r})iTE_2}$$

with ϕ_1 and ϕ_2 the phases of images 1 and 2. Defining the phase map due to inhomogeneities as

$$\Delta\phi = \phi_2 - \phi_1$$

this can be rewritten as

$$\Delta\phi = 2\pi\Delta B_0(\mathbf{r})(TE_2 - TE_1)$$

from which it follows that

$$\Delta B_0(\mathbf{r}) = \frac{\Delta\phi}{2\pi(TE_2 - TE_1)} \quad (9)$$

which in essence is the same as Equation 8.

2.5 MRI Sequences: TSE and MRF

2.5.1 Turbo Spin Echo

In the conventional SE sequence, the time between echo time $t = TE = 2\tau$ and $t = TR$ is empty. Turbo Spin Echo (TSE) exploits this dead time by repeating the 180° pulses to induce multiple echoes. When the gradient is varied between the echoes, multiple lines in k-space can be filled, thus reducing imaging time. This is shown schematically in Figure 1. The 180° pulses at $t = 3\tau, 5\tau$, etc. induce rephasing of the signal at echo times $t = 2TE, 4TE$, etc. The number of spin echoes acquired during one TR is called the echo train length (ETL).

Due to T_2 decay, the signal amplitude (which is proportional to e^{-t/T_2}) decreases over time [9], [14], resulting in a lower signal for echoes towards the end of the echo train. Therefore, often an ordering is made in which lines are put into k-space. There are multiple ways of doing this; in our case centric filling is applied. As the center of k-space predominantly determines the imaging contrast, these lines are sampled at the beginning of the train, while the lines in the periphery of k-space are sampled at the end of the train.

The T_2 decay also puts a limit to the ETL that can be used: depending on the tissues that are imaged and the desired SNR, the ETL can be very long or relatively short, as shown in [4].

2.5.2 Magnetic Resonance Fingerprinting

Underlying quantitative imaging is the concept that the combination of tissue parameters result in a unique signal evolution when using an appropriate acquisition scheme. Magnetic Resonance Fingerprinting (MRF) is a quantitative imaging method that can map several parameters at once, like the relaxation parameters T_1 and T_2 , proton density and sometimes additional parameters such as B_0 , B_1 , T_2^* or perfusion parameters [15]–[17].

The resulting signal evolution ('fingerprint') can be matched to a predefined dictionary of predicted signal evolutions. A schematic overview of the MRF principle is shown in Figure 2.

Acquisition schemes

The acquisition scheme that is used, is one in which the acquisition parameters, like the echo time (TE), repetition time (TR), or flip angle (FA), are continuously varied [15], as can be seen in Figure 2A. This leads to spin history being contained in the measured signal. [19]. In the low-field implementation

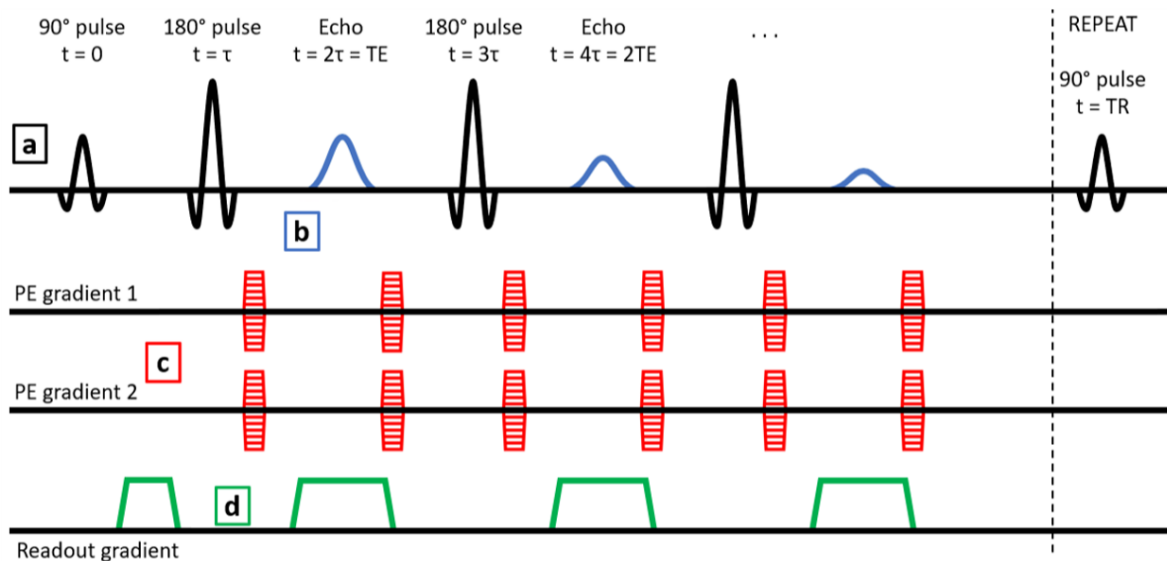


Figure 1: The Turbo Spin Echo sequence for an echo train length of 3, where the dead space between repetitions of the 90° pulse is filled with the acquisition of additional echoes. Observe the repetition of the 180° pulse at regular intervals (a), the decaying amplitude of the spin echo over time (b), the variable phase encoding gradients (c) and the repeated readout gradient (d).

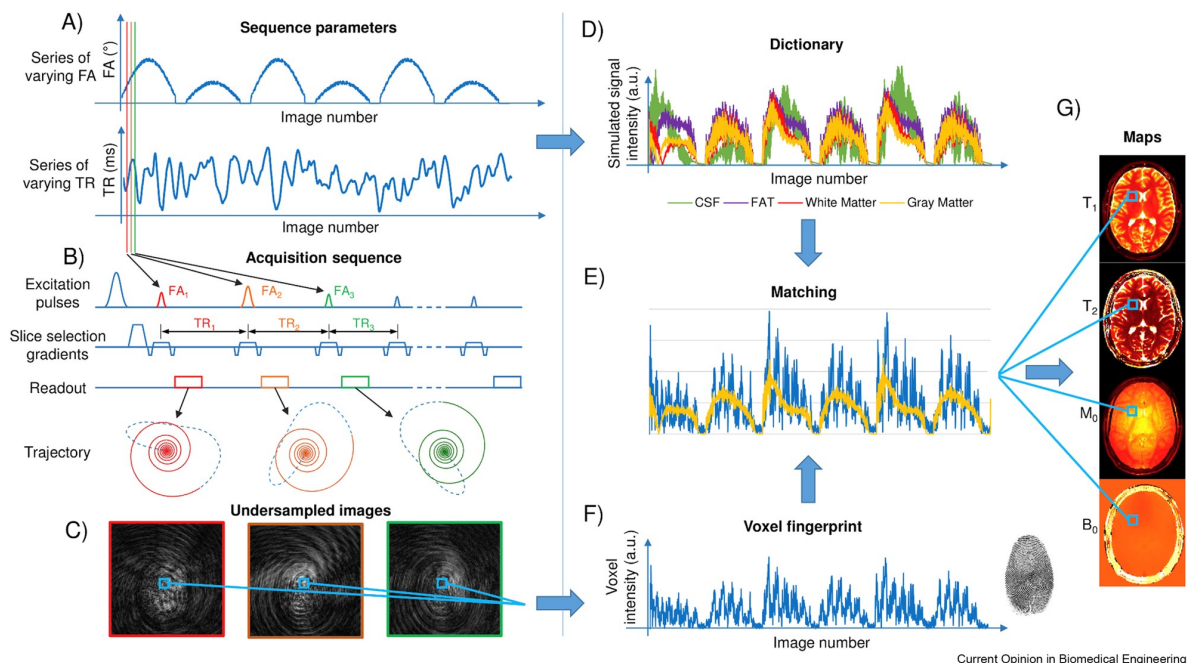


Figure 2: The working principle of MRF with a variable FA and TR in spiral imaging. Figure from [18].

currently in use at the LUMC, only the flip angle is varied, as the flip angle has the largest impact on the signal. The sequence is based on an unbalanced SSFP (steady-state free precession) sequence, also called FISP (fast imaging with steady-state free precession). This sequence is more robust to B_0 inhomogeneities than the original balanced SSFP sequence [20].

Data acquisition: Undersampling

Fully sampling a 2D or 3D volume requires one flip angle train per readout line, thus dramatically increasing the imaging time. A solution to this problem can be found in undersampling the data. This is illustrated in Figure 2C.

Generally, a spiral sampling pattern is used [16], [18], which is flexible regarding undersampling. A spiral sampling pattern can have a higher sampling density towards the center of k-space so that most global contrast features are captured, while acquiring less of the detail-defining data from the periphery of k-space. Additionally, the artifacts introduced by undersampling are noise-like, to which the dictionary matching is relatively insensitive. However, spiral imaging is sensitive to B_0 inhomogeneity, introducing blurring and distortion in all imaging planes [21], [22]. Therefore, when B_0 inhomogeneities are strong, a Cartesian sampling pattern is preferable.

Data reconstruction

When using Cartesian sampling, the undersampling artifacts that are introduced have a more structured nature compared to spiral sampling [15], [16]. This means that the artifacts will not be filtered away in the dictionary matching step, and thus requires an improvement of data quality before matching. A way to do this at high field (7T) is using matrix completion (MC), which outperforms other methods like Compressed Sensing (CS) [19], [23], [24]. It can be assumed that the same principle holds at low field strengths. This method exploits the sparsity in the singular value domain, which is possible because of the low rank due to the high temporal correlation introduced by the flip angle train [25].

The undersampling scheme for Cartesian imaging can be calculated using a variable density scheme [26]. In this scheme, the center region of k-space is fully sampled, providing a kind of calibration data which can be used later on for matrix completion. The outer region of k-space is randomly sampled.

Dictionary matching

The final step is matching every signal evolution (also called voxel fingerprint, Figure 2F) from the reconstructed data to the predefined dictionary (Figure 2D). This dictionary is built using appropriate signal models, generally by simulating Bloch equations or by using the extended phase graph formalism [18]. One of the most straightforward matching methods works by using pattern recognition models (e.g. maximizing the inner product of the measured signal and the dictionary entry [16], [18], [19]). This matching step has the additional advantage of filtering out many signal variations which are uncorrelated to the signal evolution, for example making it less sensitive to motion [15].

B_0 mapping in fingerprinting

The flip angle does not influence the phase of the image, but the echo time does, as the echo time determines the degree to which the inhomogeneities influence the phase of the signal. By alternating two different echo times during the flip angle train, the acquisition can be split up into two datasets belonging to two different echo times. By again comparing the phase of the resulting images, a B_0 map can be obtained [27].

3 Methodology

This section describes the methods and experiments designed during the thesis project. First, the interleaved B_0 mapping sequences for TSE and MRF are introduced, followed by a description of a method to correct the MR data. Finally, some experiments are described to test the mapping sequence and correction algorithm.

3.1 MRF Simulations

In order to investigate the influence of B_0 inhomogeneity on the fingerprinting sequence, a simulation has been designed, implementing the model-based distortion equations given in section 2.2. These simulations have been done in 2D to limit the computation time. The goal of these simulations is to see how inhomogeneity affects the fingerprint image, especially with regarding the estimated tissue T_1 and T_2 values.

3.1.1 Phantom design

For the simulations, a modified Shepp-Logan brain phantom was used [28], showing cerebral spinal fluid (CSF), gray matter (GM), white matter (WM), fat and muscle. The presence of muscle in a brain phantom is unconventional, but it has been added to merely investigate the effect on low- T_2 tissues, e.g. for applications in the knee.

Previous in-vivo measurements have been done at low field to find T_1 and T_2 at 50mT [29]. For fat, CM, WM, CSF and muscle, respective T_1 values of 130, 327, 275, 3695 and 171 ms have been used. Corresponding T_2 values are 90, 102, 102, 1584 and 39 ms. An overview of the phantom with the tissues and the resulting proton density, T_1 and T_2 contrast can be found in Figure 3.

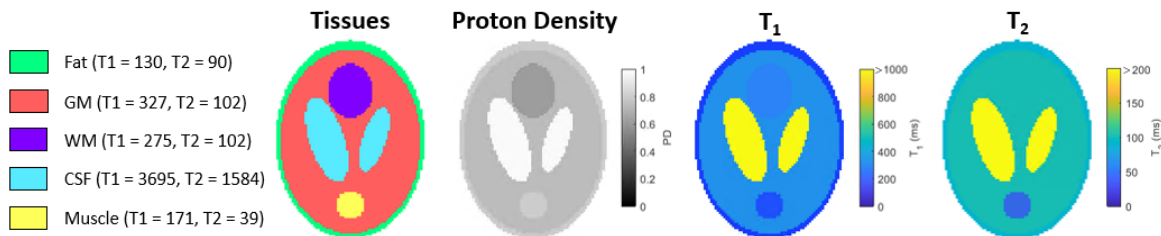


Figure 3: Showing the phantom used for the simulations, including used T_1 and T_2 values. The different tissues are highlighted.

Masks for each of the tissues have been made, and used as an input to the distortion simulation as well. These masks were then used to estimate the tissue values after distortion. This way, no additional thresholding or other segmentation method is needed, which is beneficial as for example T_1 and T_2 of GM and WM are very similar. Three different types of B_0 maps were examined:

- a homogeneous B_0 map, constant off-resonance of 667 Hz, corresponding to a shift of one pixel (bandwidth = 20kHz, $n = 30$ pixels);
- an inhomogeneous B_0 map, derived from a B_0 measurement in the 50mT scanner, with a maximum off-resonance of 2880 Hz (corresponding to a shift of around 4.3 pixels).
- an inhomogeneous B_0 map with a maximum off-resonance of 2880 Hz, and a linear time-dependence of 100 Hz/s. This is much more than realistically expected, but otherwise the effects will likely not be visible at this resolution, with a large bandwidth per voxel.

The total simulated acquisition time was 111.8 s.

3.2 Interleaved B_0 mapping

As imaging is done at low field, the signal is hardly influenced by susceptibility effects, and thus is relatively smooth, mostly containing low-frequency elements. This means that only acquiring the center of k-space, with the low frequencies, suffices. Additionally, the B_0 map is not likely to have high-frequency temporal components, as the heating of the magnets has a delaying effect. Therefore, sequences for TSE and MRF have been designed that map B_0 at a low resolution at regular intervals during image acquisition.

3.2.1 Interleaved B_0 mapping for TSE imaging

In order to acquire low-resolution B_0 maps during image acquisition, a simple interleaved TSE sequence was developed. This sequence is illustrated schematically in figure 4. The sequence is built as follows:

- Figure 4a: the image acquisition is broken into n blocks of echo trains. Every block contains an integer number of trains. This means that when the number of echo trains divided by the number of blocks is non-integer, some blocks will contain one echo train more than the others.
- Figure 4b: between the image acquisition blocks, and at the beginning and the end of the sequence, a B_0 map is acquired. The data of these $n + 1$ B_0 maps is stored separately.
- Figure 4c: the B_0 map is measured by repeating standard echo trains (yellow) with a shifted readout (red). The B_0 -induced phase shifts can be derived by comparing these echo trains.

The B_0 map is computed from the phase difference between the normal and shifted acquisitions, see Equation 8. This map is only reliable at image locations where there is signal, leading to an inaccurate B_0 estimation for voxels outside the phantom or patient. Therefore, spherical harmonics fitting (SH) will be applied. This also serves to extrapolate the B_0 field where needed.

3.2.2 Interleaved B_0 mapping for fingerprinting

As mentioned in section 2.5.2, the alternating echo times provide data to estimate a B_0 map. However, if all data is combined this map is an average over the entire imaging sequence and thus is not dynamic. Moreover, this map is made by using data from the entire k-space, thus having a higher resolution than required for a low resolution B_0 map.

In order to acquire multiple B_0 maps during a normal fingerprinting acquisition, the data from the alternating echo shifts can still be used, but in a different way. Generally, the scanner uses as input the flip angle and the corresponding k-space point (or the gradients belonging to that point) for all trains. The center of k-space is typically not measured during one flip angle train, but spread out over different flip angle trains, as a Cartesian sampling scheme is applied. By designing a special ordering, a flip angle train, hereafter called the B_0 train, can be inserted at regular intervals which only acquires the center lines, enabling B_0 mapping over time. This interleaved B_0 mapping is illustrated in Figure 5, and shows many similarities compared to the TSE approach presented in Figure 4.

In order to create a B_0 map, the special B_0 train should sample the center of k-space twice, once for each echo time. There is some freedom in which regions are sampled. One could choose a fixed resolution, and fill the rest of the available flip angles with additional (randomly sampled) k-space data from the outer regions of k-space. Other options include maximizing the B_0 map resolution given the FA train length, or sampling certain points multiple times, to improve accuracy by averaging. For a flip angle train of length 240, 120 lines per TE can be filled, resulting in a maximum square center size of 10x10. Examples of trajectories for normal flip angle trains and B_0 trains are shown in Figure 6.

From the k-space data acquired by a B_0 train, an image for TE_1 and an image for TE_2 can be reconstructed, see Figure 6. Because the data points are acquired at different flip angles, the magnitude of the image will not be representative. The flip angle however does not influence the phase. Therefore, from the phase difference between these images, a B_0 map can be derived, in accordance with Equation 9. Like in TSE, SH fitting will be used to extrapolate the field to outside the phantom to remove noise.

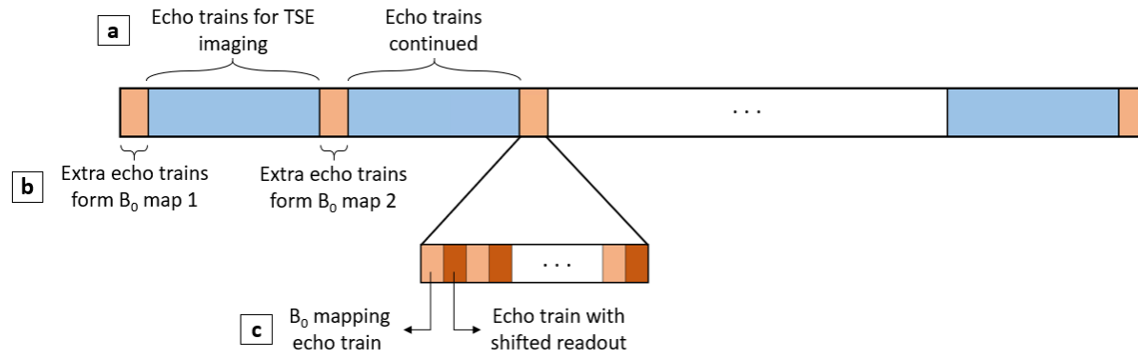


Figure 4: Schematic of interleaved B₀ mapping TSE sequence, showing a) the TSE image acquisition, broken up in a number of parts; b) the B₀ mapping blocks at regular intervals, note that each block is a B₀ map and c) a close-up of the B₀ mapping sequence, where echo trains are repeated with a readout gradient shift, to introduce B₀-induced phase shifts.

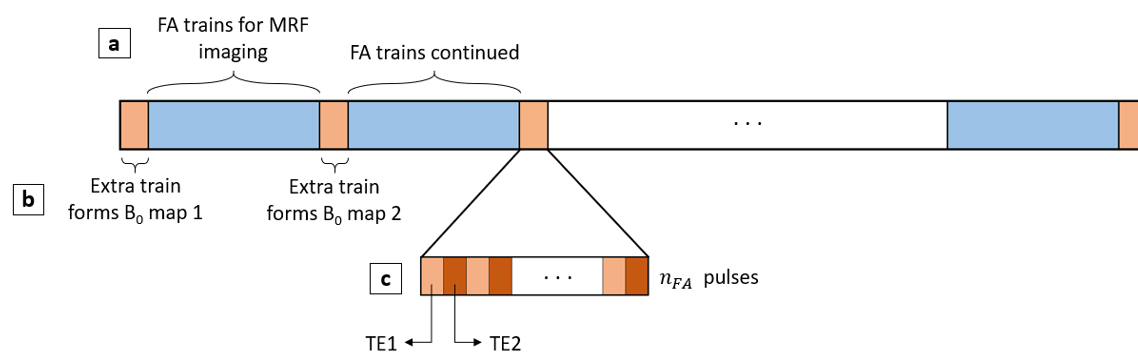


Figure 5: Schematic of interleaved B₀ mapping MRF sequence, showing a) the MRF image acquisition trains; b) the B₀ mapping trains at regular intervals c) a close-up of the B₀ mapping train, where an alternating echo time is used along the MRF pulses.

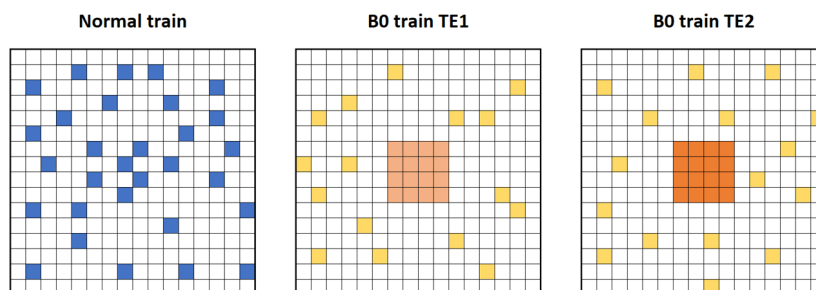


Figure 6: Example of FA trajectories in MRF. Left shows the k-space point sampled for a normal flip angle train, randomly sampled, the middle and right B₀ train trajectories for echo times 1 and 2 with fully sampled center of k-space, randomly sampled outer regions.

At places where there is not enough signal, the B_0 map will not be accurate. Therefore, masking is required. In TSE, this was done based on the intensity of the image acquired during the B_0 acquisition block. Because of the non-representative image that is formed by one MRF train, masking the B_0 map based on B_0 train images will not work perfectly. Therefore, the mask was created based on the mean over the FA dimension of the high resolution image, and resized to fit the low resolution image.

3.2.3 B_0 map acquisition parameter optimisation in TSE

When acquiring the B_0 maps in the interleaved sequence at the same resolution as the TSE image acquisition, the scan time would increase by the number of maps, $n_m \times 100\%$. Therefore it is relevant to find out what can be altered such that the additional scanning time is as low as possible. These measurements will be done using the TSE sequence.

- B_0 map resolution and number of maps: Two possibilities will be compared: an 8x8 center and a 16x16 center. Also, repeated acquisitions of 5 and 10 maps, equally spread along the duration of the TSE sequence, will be compared. Note that the acquisition time of one map scales with the square of the size of the center.
- Repetition time (TR): It might be advantageous to image under steady state conditions by increasing TR [9]. This ensures that there is no spin history in the longitudinal or transverse magnetization. An alternative to reach the same effect may be the introduction of dummy trains. These two methods will be compared, as well as two different values for TR: one experiment with 1.5 s and 4 s for the apple phantom (estimated resp. about 1 and 2.5 times T_1), one experiment with 1 and 2 s for the Hyperfine phantom (resp. 1.5 and 3 times T_1).
- Readout shift: t_{shift} affects the phase effects introduced in the image, as a larger shift will have a stronger effect. Two different shifts will be compared, $150\mu s$ and $500\mu s$.

3.3 Image correction

Research has shown that when considering image quality, model-based reconstruction yields better results [6], as CPR will fail in regions with large B_0 inhomogeneities. When B_0 is constant, all data can be corrected for at the same reconstruction step. When B_0 is time-dependent however, for every readout line there is a different B_0 , and thus a separate reconstruction has to be done. This increases reconstruction time. For this purpose therefore, model-based reconstruction may become too time-consuming, which is why CPR is used in this project, unless otherwise mentioned.

The correction step has been implemented using a fast implementation of the CPR algorithm. The B_0 map was assumed to be constant per echo train. If echo trains experience the same B_0 therefore, they can be corrected for in the same iteration, which saves image reconstruction time.

3.3.1 Image correction pipeline for TSE

The correction is performed before the normal image reconstruction. The pipeline consists in general of several steps:

- Step 1: Calculate B_0 from the interleaved B_0 acquisition. Use SH fitting.
- Step 2: For each echo train, find the B_0 maps acquired before and after this train, using the k-space trajectory file.
- Step 3: Interpolate to get the right B_0 map, depending on the method, see the descriptions below.
- Step 4: Use the fast CPR implementation on this train with the right B_0 map to correct the data, as discussed above.
- Step 5: Continue with normal reconstruction, which is a Fourier Transform for TSE.

As described in section 2.2, image correction is computationally expensive. Therefore, it is useful to find out how accurate the B_0 estimation should be to obtain good results. Therefore, three methods will be compared for TSE imaging:

- Method 1: Correction using the average of the B_0 maps. This is equivalent to inhomogeneous correction without frequency drift. This method is fastest, requiring only one CPR computation, and takes (depending on image size) around one second.
- Method 2: Correction using piece-wise correction: all echo trains between two acquired B_0 maps will be corrected at the same time. The B_0 map used for this correction is the average of the B_0 maps before and after this block of echo trains. Computation time depends on image size and number of B_0 maps, and takes in the order of seconds.
- Method 3: Correction of each echo train separately. The B_0 map used for the correction of an echo train is a linear interpolation between the B_0 maps closest to the echo train. Computation time, depending on image size and ETL, takes in the order of minutes.

3.3.2 Image correction pipeline for MRF

In MRF, the correction is much more time-consuming than in TSE. Whereas in TSE the entire echo train, or even a group of echo trains, can be corrected for simultaneously, this is not possible in MRF. In MRF, every FA has its own k-space, thus correction for one flip angle train needs to be done for every FA separately. This increases the reconstruction time by a factor of nFA and results in an extremely long reconstruction time with the current implementation on the current system.

Therefore, an alternative is proposed for MRF correction. Assuming the drift is sufficiently homogeneous to not cause artefacts due to its inhomogeneity (meaning that the drift values in every map are mostly smaller than the bandwidth per voxel), the correction could be split into two parts, resulting in the following steps:

- Step 1: Calculate B_0 maps from each of the B_0 trains.
- Step 2: Calculate the corresponding drift maps, using as a reference map the center one. Use SH fitting of the 0th order on the drift result to get homogeneous estimations.
- Step 3: For each flip angle train, correct the data with the relevant homogeneous B_0 map. As seen in chapter 2, a homogeneous B_0 is just a linear phase shift in k-space. This can be implemented very efficiently.
- Step 4: Take one slice (readoutxPE1, acquired at 240 time points) of the 3D volume and use the model-based reconstruction which has been implemented for 2D MRF (see [6]) and perform correction for inhomogeneous B_0 , using a B_0 estimated from the drift-corrected data.
- Step 5: Perform dictionary matching.

Correction on the 3D volume is possible, though that would increase reconstruction time by a factor of the number of PE2 steps.

Three reconstruction methods will be compared:

- Method 1: Inhomogeneous correction on the distorted data, thus only correcting for static B_0 inhomogeneities, assuming one average B_0 map.
- Method 2: Drift correction on the distorted data, thus only correcting for a zero-order B_0 drift, see step 2 in the description above.
- Method 3: A combination of methods 1 and 2, as described above, thus correcting both for an approximation of B_0 drift and for B_0 inhomogeneities.

3.4 Experimental setup

3.4.1 Phantoms

In the experiments, several different phantoms were used, depending on their availability and the aim of the measurement. The phantoms are:

- An approximately spherical ball with a diameter of 12.5 cm, see Figure 7a. The ball is useful for checking distortion correction, as the shape is known. T_1 and T_2 are both measured at 358 ms.



Figure 7: Phantoms used in the experiments. Note that the ball in a) is not completely spherical.

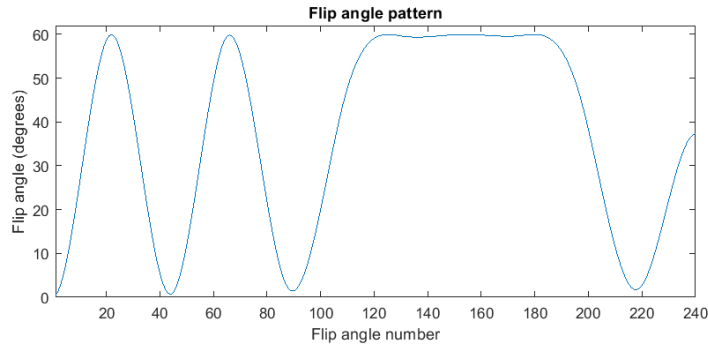


Figure 8: The flip angle pattern used in the MRF measurements.

- A commercial phantom created by Hyperfine[®], see Figure 7b. The diameter is 12.2 cm, the length 14.3 cm. This phantom is useful for checking both distortion correction and image quality in terms of detail visible in the image. T_1 and T_2 are both measured at 670 ms.
- An apple with a diameter of around 8 cm. This phantom was used as a more realistic homogeneous phantom for some experiments. At 1.5 T, T_1 is about 1500 ms, T_2 about 200 ms [30]. Values at low field are unknown.

3.4.2 Measurements

Table 1 describes the measurements that have been done, in the order in which they will be presented in section 4. Those measurements marked with 'Yes' in the column 'Heating?' are measurements to simulate the heating that would take place in an in-vivo experiment, to increase the B_0 drift. This was done using warm water bottles with a temperature of around 40 °C, placed near one end of the scanner. The scanner was closed on both sides to keep most of the heat inside. As the heating of the scanner takes some time, there was a time interval of a couple of minutes between the placement of the bottles and the starting of the scan.

The flip angle pattern, optimized for MRF imaging at low T_1 and T_2 , is displayed in Figure 8.

3.4.3 Hardware

System specifications of the magnet, spectrometer and gradient amplifiers can be found in [4]. For a part of the measurements, different amplifiers have been used, but they did not influence the image quality. Simulations and image reconstructions were performed on a 64-bit computer with an Intel[®] Core i3-4160 processor and 16 GB RAM.

Table 1: Acquisition parameters for the TSE and MRF measurements in the order in which they are presented in the results. The field of view (FOV) is given in readout x phase encoding 1 (PE1) x phase encoding 2 (PE2). The bandwidth (BW) in the readout direction was 20 kHz. For TSE: n_d is the number of dummy trains, n_m the number of B_0 maps, t_{img} the acquisition time of the image without B_0 mapping, t_{B_0} the added acquisition time for the B_0 maps. Note that for B_0 mapping, the volume should be acquired twice. For MRF: n_{fully} is the side of the center square that is fully sampled, n_{random} the total number of randomly sampled lines per phase encoding direction, $n_{t,img}$ the number of trains during image acquisition, n_{t,B_0} the number of B_0 trains (equivalent with the number of maps). t_{img} and t_{B_0} are defined like in TSE. The length of the FA train was always 240, TE₂-TE₁ 150 ms, the inversion delay 24 ms and the repetition delay 500 ms.

TSE														
#	Phantom	FOV (mm)	Grid size	TR (s)	ETL	$t_{shift}(\mu s)$	n_d	n_m	Map size	Heating?	$t_{img}(s)$	$t_{B_0}(s)$	% increase	Used for:
1	Hyperfine	150x150x210	100x50x35	1	32	250	0	10	100x16x16	Yes	54.7	160	292	Map size / #maps comparison Distortion correction
2	Hyperfine	150x150x210	100x50x35	1	32	250	0	5	100x16x16	Yes	54.7	80	146	Map size / #maps comparison Distortion correction
3	Hyperfine	150x150x210	100x50x35	1	32	250	0	5	100x8x8	Yes	54.7	20	36	Map size / #maps comparison Distortion correction
4	Hyperfine	150x150x210	100x100x70	1	32	250	0	5	100x16x16	No	54.7	80	146	TR/dummy comparison
5	Hyperfine	150x150x210	100x100x70	2	32	250	0	10	100x16x16	No	109.4	160	146	TR/dummy comparison
6	Hyperfine	150x150x210	100x100x70	1	32	250	5	5	100x16x16	No	59.7	80	132	TR/dummy comparison
7	Apple	120x120x120	60x60x60	1.5	16	150	0	10	60x16x16	No	337.5	480	142	TR comparison
8	Apple	120x120x120	60x60x60	4	16	150	0	10	60x16x16	No	900	1280	142	TR comparison
9	Ball	200x200x200	100x8x8	1.5	16	150	0	5	100x16x16	No	6	240	x	Readout shift comparison
10	Ball	200x200x200	100x8x8	1.5	16	500	0	5	100x16x16	No	6	240	x	Readout shift comparison
11	Ball	180x180x180	120x120x120	0.8	16	150	0	10	120x16x16	Yes	720	256	36	Distortion correction
12	Hyperfine	150x150x210	100x100x70	1	32	250	0	10	100x16x16	Yes	218.8	160	74	Distortion correction
13	Hyperfine	150x150x210	100x100x70	1	32	250	0	10	100x8x8	Yes	218.8	40	18	Distortion correction

MRF														
#	Phantom	FOV (mm)	Grid size	TR (ms)	n_{fully}	n_{random}	$n_{t,img}$	n_{t,B_0}	Map size	Heating?	$t_{img}(s)$	$t_{B_0}(s)$	% increase	Used for:
1	Ball	170x150x99	68x60x33	12	8	8	528	27	68x8x8	No	1797	91.9	5	Distortion correction
2	Ball	170x150x99	68x60x33	12	8	8	528	27	68x8x8	Yes	1797	91.9	5	Distortion correction
3	Hyperfine	170x150x99	68x60x33	12	4	3	231	12	68x10x10	Yes	786	40.8	5	Distortion correction

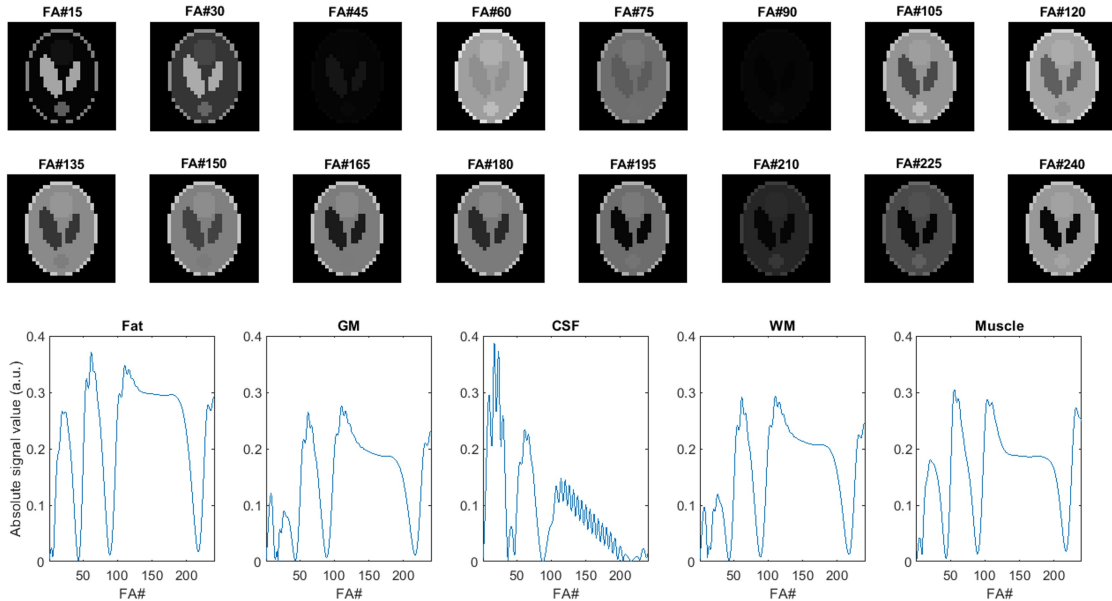


Figure 9: Simulation results: The change in image contrast during the MRF flip angle train, for the phantom and for the five separate tissues.

4 Results

This section describes the results of the measurements performed during this project. First, simulation results will be shown, followed by the results of measurements studying important B_0 mapping parameters. Also the distortion correction results are shown and compared, for both TSE and MRF sequences.

4.1 MRF Simulation

Figure 9 shows a simulation of the signal intensity for several different flip angles, illustrating that image contrast changes over time due to the varying flip angle. The plots on the bottom of the figure show fingerprints for each of the five tissues. Note that at flip angles 45 and 90 for example, the signal is nearly zero for all tissues (see also Figure 8), which explains the black images. Figure 10 shows the distorted phantom signal for the three distortion types for several flip angles. The homogeneous map results in a pixel shift, as expected from the B_0 value chosen. The inhomogeneous map results in distortions, and the time-dependent map clearly introduces additional blurring. Figure 11 shows the distorted phantoms and the corresponding masks (including matched T_1 values), showing that the proposed masks can be used to evaluate the relaxation times estimated from the distorted images.

Figure 12 shows the reference T_1 and T_2 maps, and the maps resulting from the simulations of the three types of B_0 distortions in the top rows of the first and second part of the figure, respectively. The bottom rows of the two figure parts show the corrected images, using the same approach as is later used for the real experiments. It is visible that each B_0 map produces a different kind of distortion in the T_1 map, similar to what was observed in the source images in Figure 10. Note that the colorbar is clipped, because of visibility reasons.

Figure 13 shows boxplots of the percentual and absolute deviation in T_1 values for each tissue before and after correction for the three distortion types: homogeneous, inhomogeneous and time-dependent B_0 . Note that the dictionary has a resolution of 5 ms for the matched T_1 and T_2 , which

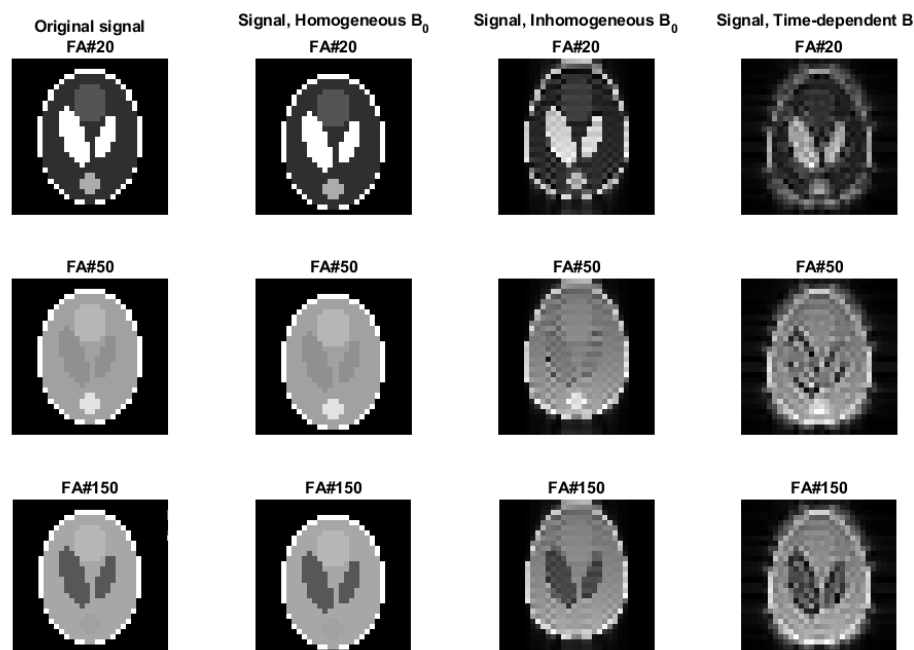


Figure 10: Simulation results: The phantom signal for different distortion types and flip angles.

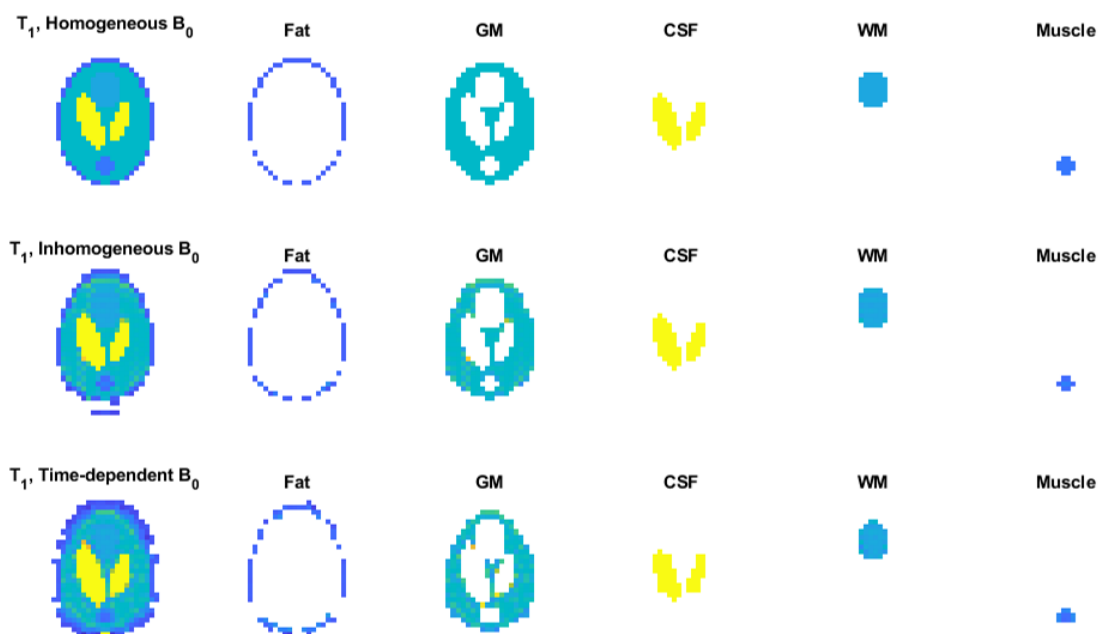


Figure 11: Simulation results: T_1 maps for the three distorting methods and the corresponding tissue masks.

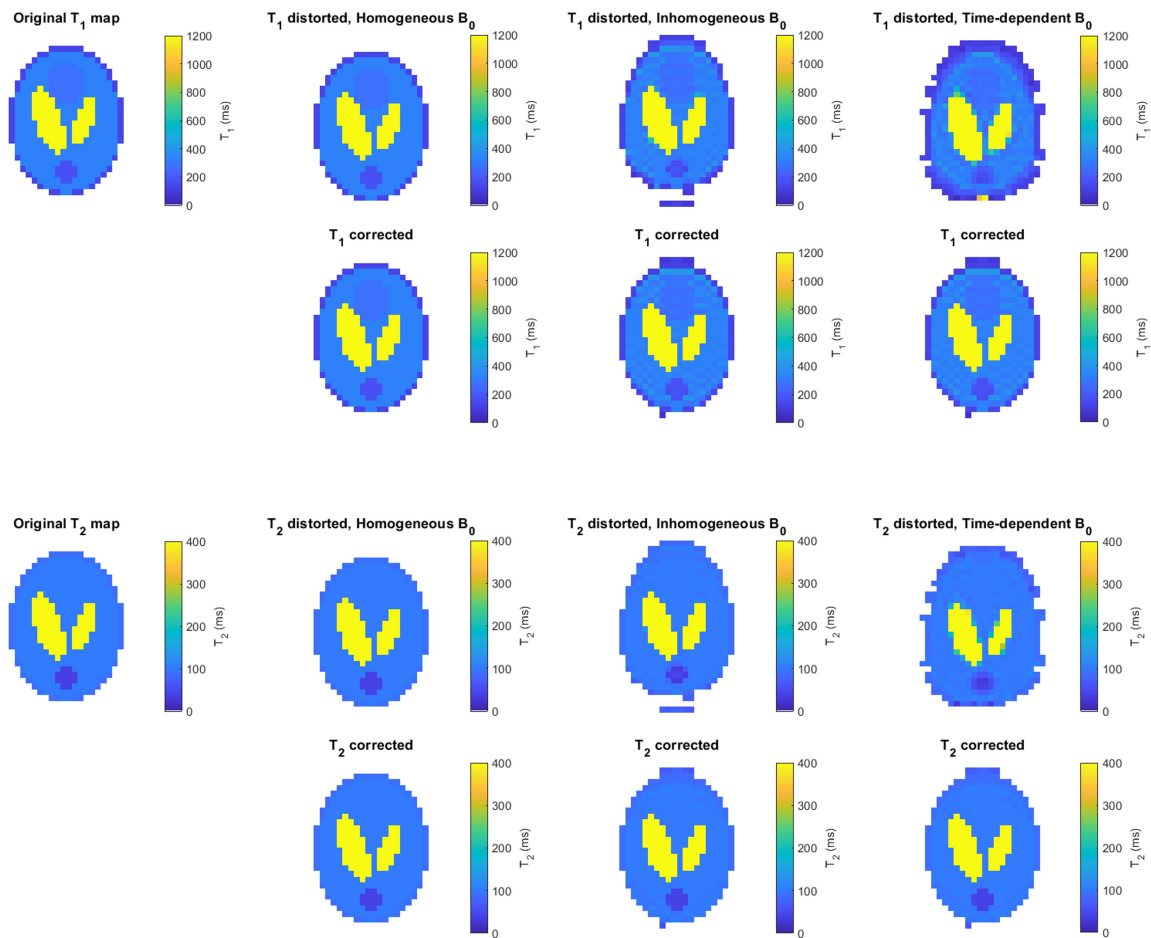


Figure 12: Simulation results: The original, distorted and corrected T₁ and T₂ maps.

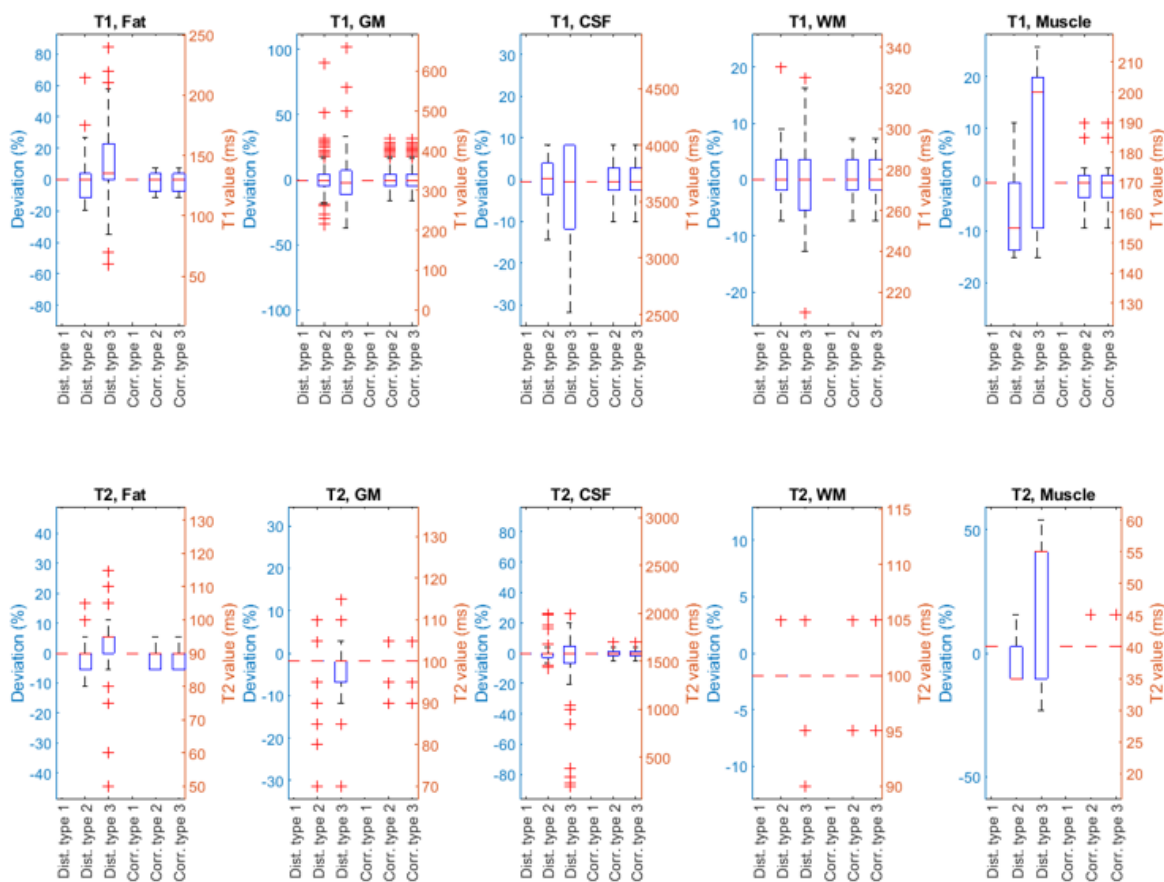


Figure 13: Simulation results: The spread in T_1 and T_2 values for the three distortion types, including the spread after correction. Type 1 is the homogeneous B_0 , type 2 the inhomogeneous B_0 , type 3 the inhomogeneous and time-dependent B_0 .

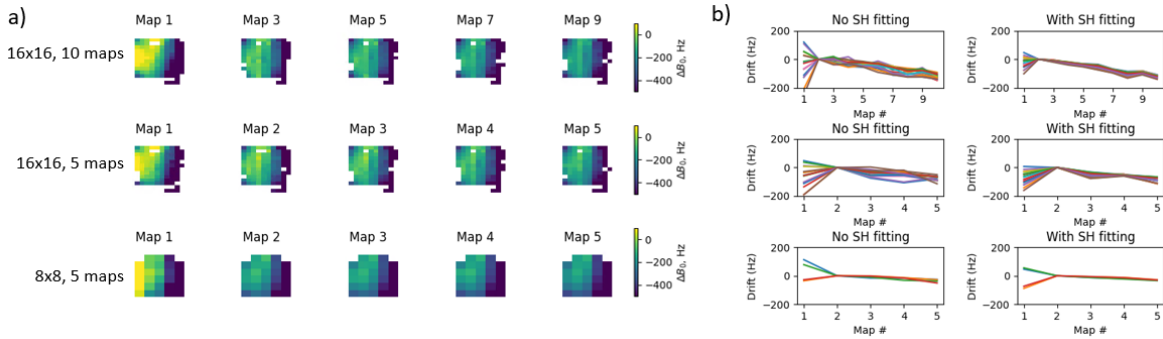


Figure 14: Measurement results for TSE imaging. a) 5 of the B_0 maps, acquired over time, in which no fitting is performed and b) the drift value of a small region of pixels of the middle readout slice. The drift plot is based on the second map, as the first map is slightly different from the rest. Also note that plot b) is shown as a function of map and not of time, and time between maps may vary between measurements. For acquisition parameters, see Table 1.

is why for example in T_2 for WM and muscle, there is a small deviation even for distortion type 1, which should not influence the parameter maps. From the figure, it can be seen that the errors in the quantitative maps decrease when applying correction, for example in T_1 for CSF, from about 5% standard deviation to 2.5% standard deviation.

4.2 Optimizing B_0 mapping parameters

B_0 map resolution and number of maps

Figure 14 shows a comparison between 5 and 10 B_0 maps, and between 16x16 and 8x8 maps, for an acquisition with the Hyperfine phantom. These measurements corresponds to measurements 1-3 in Table 1. The purpose of these measurements was to study the effect of B_0 mapping at a lower resolution than the target image acquisition, both temporally and spatially. For all three experiments, the B_0 maps show a decreasing trend over time. This is reflected in Figure 14b), where the drift values of a small region in the B_0 map are plotted as a function of map, showing changes in the B_0 field.

Repetition time

Figure 15 shows a comparison between $TR = 1$ and 2s, and adding dummy trains, for the Hyperfine phantom. It also shows a comparison between $TR = 1.5$ s and 4s for the apple. These measurements correspond to measurements 4-8 in Table 1. The purpose of these measurements was to find out whether the temporal stability of a B_0 map can be improved by making TR longer or by adding dummy trains. One can observe that SH fitting reduces the fluctuation over time. A longer TR does not significantly reduce the fluctuations, introducing dummy trains appears to give a smooth drift.

Readout shift

Figure 16 shows a comparison between B_0 maps acquired with a short readout shift ($150 \mu s$) and a long readout shift ($500 \mu s$) for a ball-shaped phantom. These measurements correspond to measurements 9 and 10 in Table 1. The image acquisition was done at a very low resolution, so that the B_0 maps were only separated by one echo train (1.5s). No external heat source was applied, minimizing the drift. Though the maps look stable, there is some drift visible in the center pixels, see Figure 16b. Increasing t_{shift} results in smaller fluctuations over time.

4.3 Distortion correction in TSE

Figure 17 shows the distorted data and the corrected data for the Hyperfine phantom. This measurement corresponds to measurement 1 in Table 1. Figure 18 shows the same results for the ball

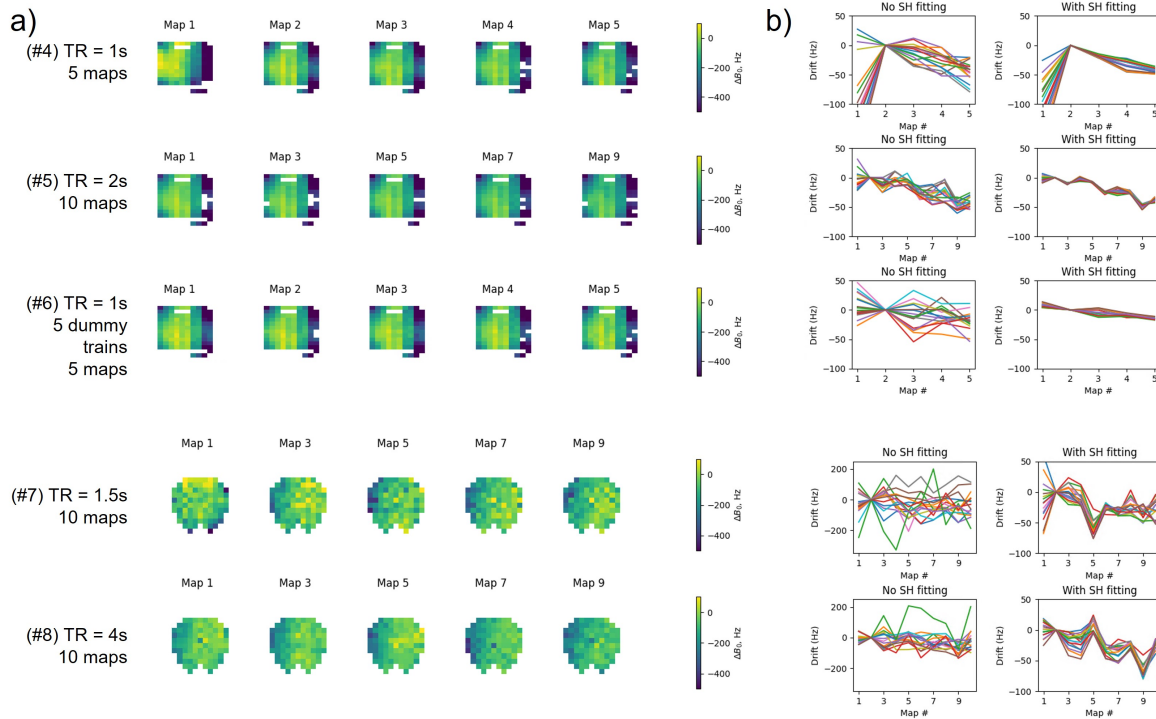


Figure 15: Measurement results for TSE imaging. Showing for the Hyperfine phantom and for the apple a) 5 of the B_0 maps, acquired over time, in which no fitting is performed and b) the drift value of a small region of pixels of the middle readout slice. The drift plot is based on the second map, as in some cases the first map is slightly different from the rest. Also note that plot b) is shown as a function of map and not of time, and time between maps may vary between measurements. For acquisition parameters, see Table 1.

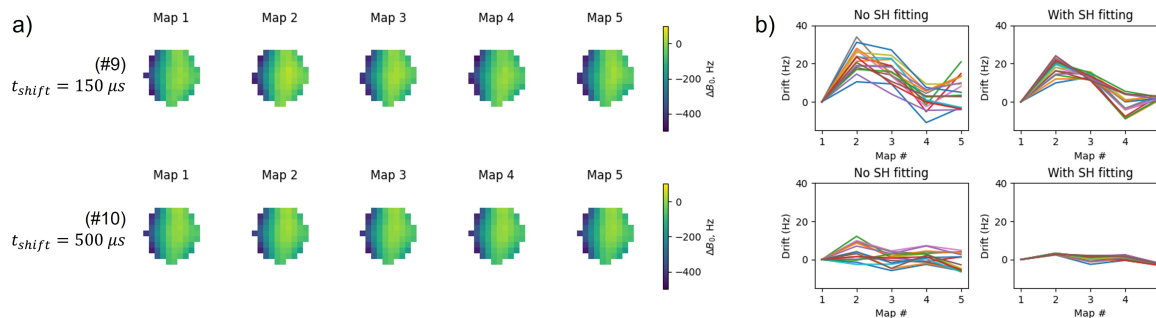


Figure 16: Measurement results for TSE imaging. Showing for the ball phantom a) 5 of the B_0 maps, acquired over time, where no fitting is performed and b) the drift value of the center 4×4 pixels of the middle readout slice. The time between measurements was the same for both measurements. For acquisition parameters, see Table 1.

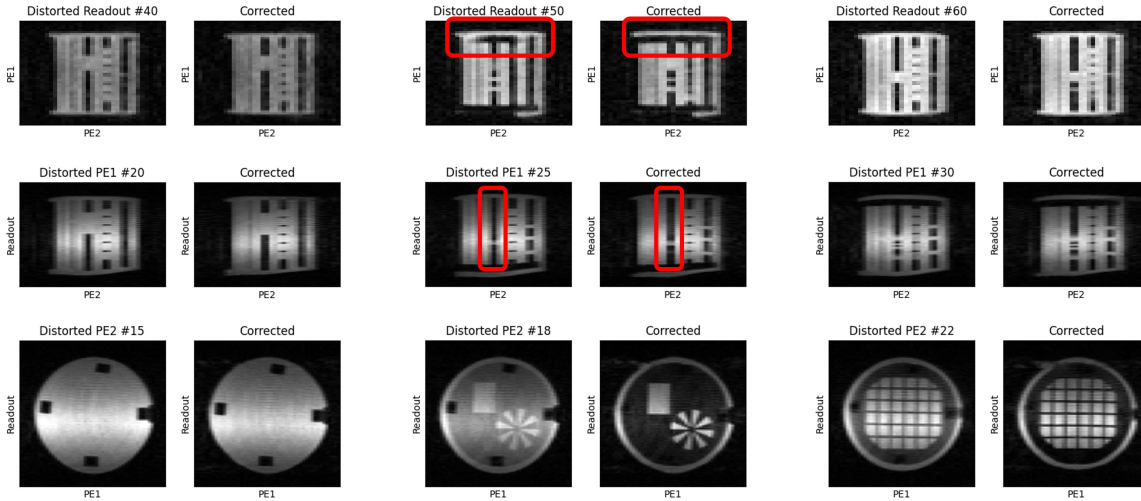


Figure 17: Measurement results for TSE imaging. Distorted and corrected data in different planes and different slices for the Hyperfine phantom. The correction is performed by processing each echo train individually. The areas circled in red show some significant improvements in image quality.

phantom, measurement 11. The data has been corrected by processing every train separately. Figure 19 shows the fitted B_0 map, the distorted data and the corrected data of this same measurement, using three different methods: correction in one block, using the mean of the fitted B_0 map over time, thus omitting the drift factor, piece-wise correction in 9 blocks, approximating the time-dependent B_0 , and correction per echo train. For more details on these methods, see section 3.3.1.

Although after correction the images become less distorted, and sharpness increases especially in the PE1 and PE2 directions (see the red markings in Figure 17), no large differences between the three correction methods are visible in Figure 19. In Figure 19, the red markings indicate artefacts that are likely to be introduced by the imperfect B_0 map visible on the left.

Figure 20 shows the same results, but for a measurement at higher resolution, $100 \times 100 \times 70$ voxels for the same FOV. For acquisition details, see measurement 12 in Table 1. Here, some improvement is visible in the time-dependent correction with respect to correction with the average B_0 , see the red markings.

Figure 21 shows the results for the ball phantom, measurement 11. In the images indicated by the red line, a clear difference is visible between the distorted and corrected images. The correction with the mean B_0 does correct for the distortion, but the ringing artefact remains. In both time-dependent reconstructions, this artefact is greatly reduced. Figure 22 shows a comparison between the correction results of different measurements (for more acquisition details, see Table 1):

- Figure 22a): grid size target image $100 \times 100 \times 70$, 10 B_0 maps of $100 \times 16 \times 16$ (Measurement 12)
- Figure 22b): grid size target image $100 \times 100 \times 70$, 10 B_0 maps of $100 \times 8 \times 8$ (Measurement 13)
- Figure 22c): grid size target image $100 \times 50 \times 35$, 10 B_0 maps of $100 \times 16 \times 16$ (Measurement 1)
- Figure 22d): grid size target image $100 \times 50 \times 35$, 5 B_0 maps of $100 \times 16 \times 16$ (Measurement 2)
- Figure 22e): grid size target image $100 \times 50 \times 35$, 5 B_0 maps of $100 \times 8 \times 8$ (Measurement 3)

Here, it is visible that in some cases, the resolution of the B_0 map does influence the correction result significantly, see the areas highlighted in red for image distortions and blurring introduced by an inaccurate B_0 .

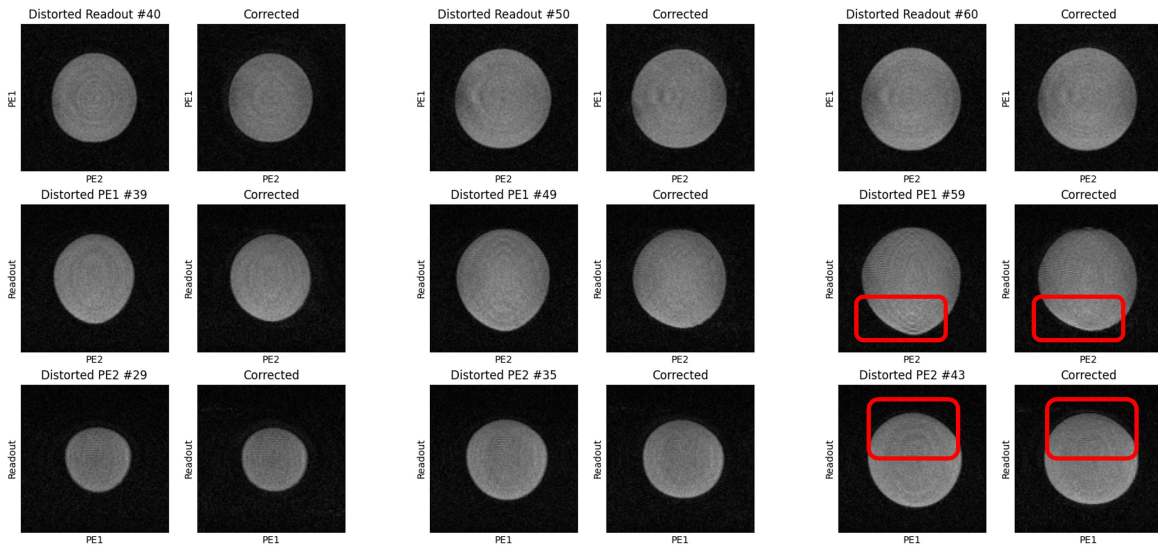


Figure 18: Measurement results for TSE imaging. Distorted and corrected data in different planes and different slices for the ball phantom. The correction is performed by processing each echo train individually. The areas circled in red show some significant improvements in image quality.

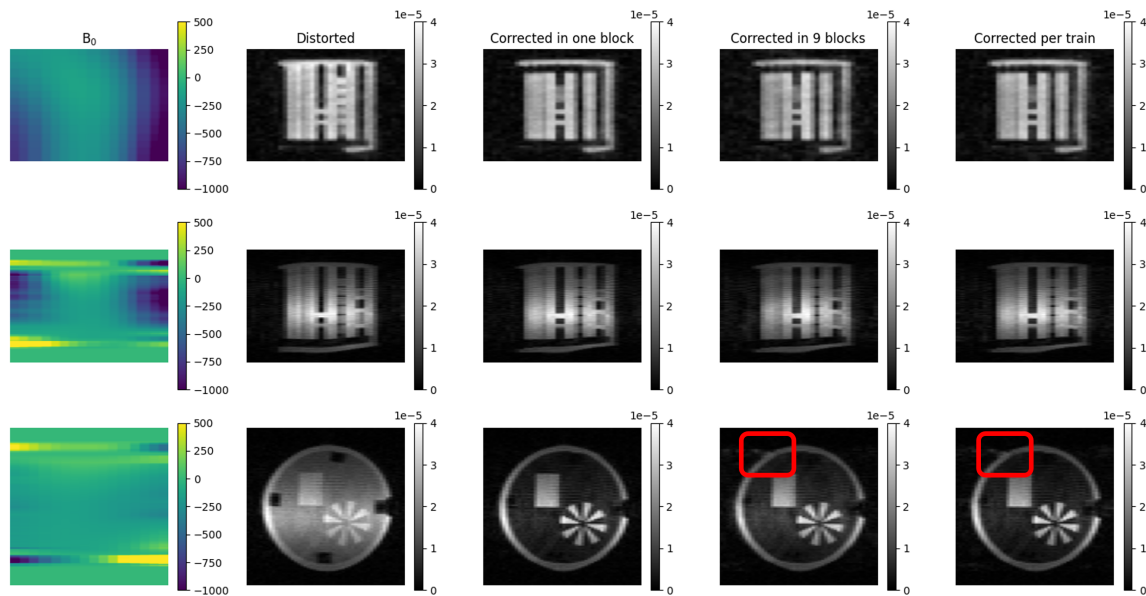


Figure 19: Measurement results for TSE imaging. A comparison between the three different correction methods for different planes, for a measurement of $100 \times 50 \times 35$ voxels. The areas circled in red show some artefacts introduced by the imperfect B_0 map visible on the left.

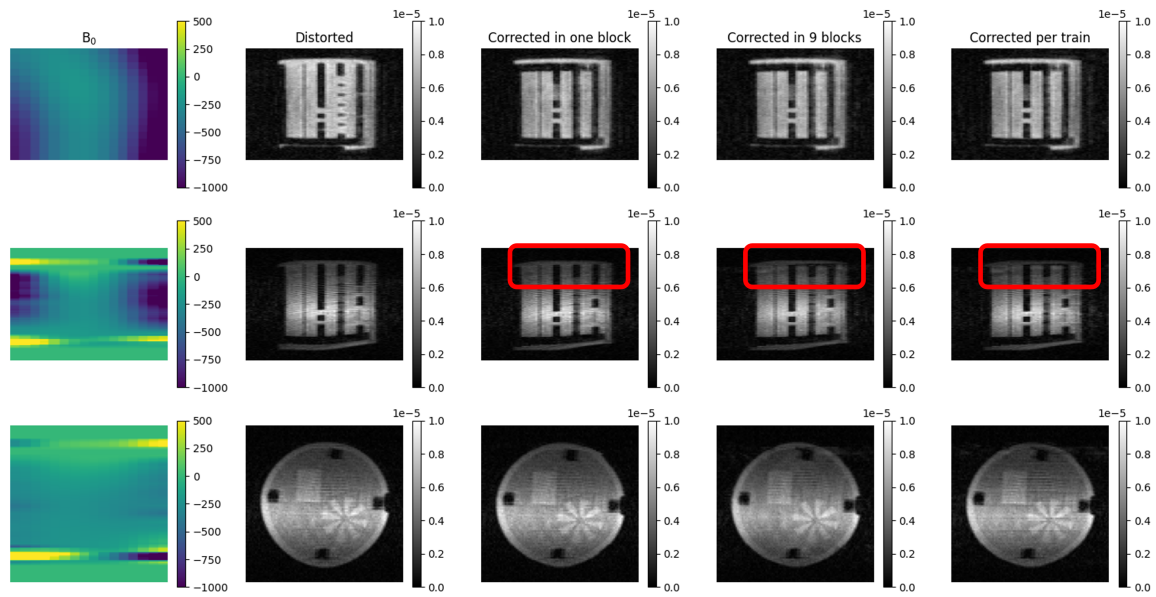


Figure 20: Measurement results for TSE imaging. A comparison between the three different correction methods for different planes, for a measurement of $100 \times 100 \times 70$ voxels. Note the increase in detail between the correction methods, highlighted with the red markings.

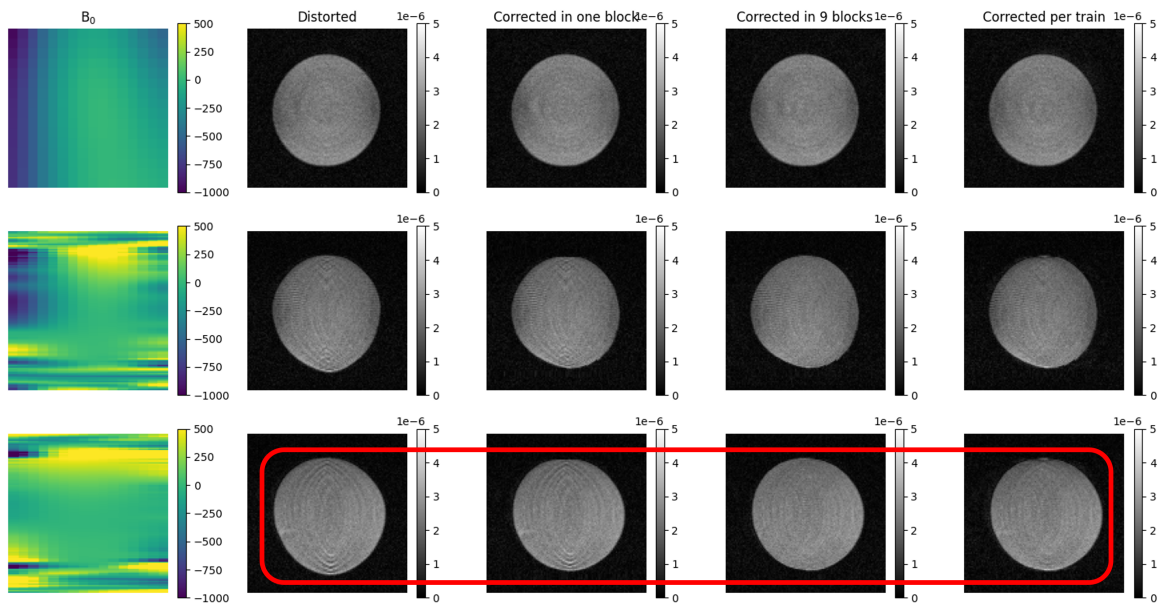


Figure 21: Measurement results for TSE imaging. A comparison between the three different correction methods for different planes, for a ball-shaped phantom with grid size $120 \times 120 \times 120$. Note the disappearance of the ringing artefact in the last two columns, highlighted with the red markings.

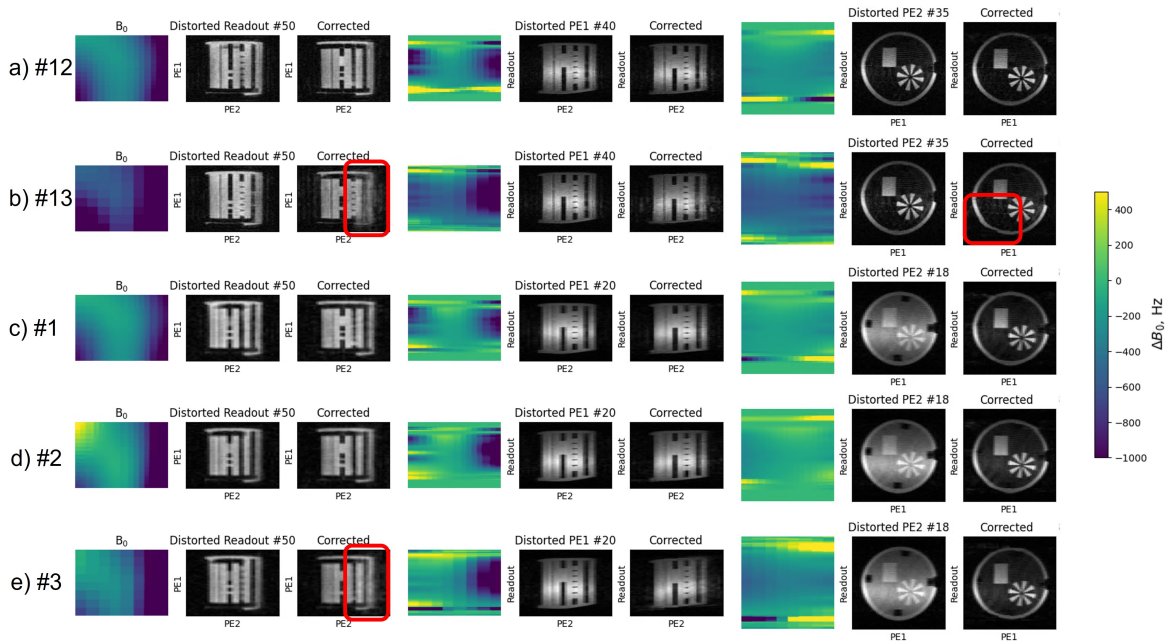


Figure 22: Measurement results for TSE imaging. Showing a comparison between the fitted B_0 , distorted and corrected images for measurements with different image resolution, B_0 map resolution and number of maps. The correction is performed by processing each echo train individually. The areas marked with red show distortions introduced by an incorrect B_0 .

4.4 Distortion correction in MRF

Figure 23 shows drift maps for TSE measurement 12, computed as the difference between subsequent maps. The drift map for map 2 with respect to map 1 looks different due to map 1 being different from the others, the same effect was observed in Figure 15. The drift is not homogeneous, but remains mostly between 20 and -50 Hz between B_0 maps. This means that for a sufficiently large BW/voxel, say roughly 100 Hz or above, it can be approximated as homogeneous as the shifts originating from these inhomogeneities are less than a voxel. This is relevant for the MRF experiments, in which the drift was assumed to be homogeneous within BW/voxel limits. From these TSE experiments, it appears that the assumption holds.

Figure 24 shows examples of images and phase maps from the B_0 trains for a ball-shaped phantom. This figure illustrates that masking based on B_0 trains will not work since the resolution is too low, and signal variations due to the flip angle are too strong. The estimated B_0 map and a fitted 0th order SH are shown, including an example of masking at higher resolution. The fold-over artefact visible in the high resolution data is caused by a too small FOV.

Figure 25 shows the resulting T_1 and T_2 maps for a 2D slice of the distorted ball and Hyperfine phantoms, and three types of correction: correction based on the average B_0 map, correction based on the time-dependent drift, and correction based on a combination of these methods. For more details on these methods, see section 3.3.2. Shown are the results for a ball phantom with and without heating applied, and for the Hyperfine phantom with heating applied. See respectively MRF measurements 1-3 in Table 1 for acquisition parameter details.

The following drift values were calculated:

- Ball, non-heated: center frequency before scanning 2.149 MHz, after scanning 2.14884 MHz, which implies a frequency drift of 160 Hz. Scan duration 31.5 minutes.

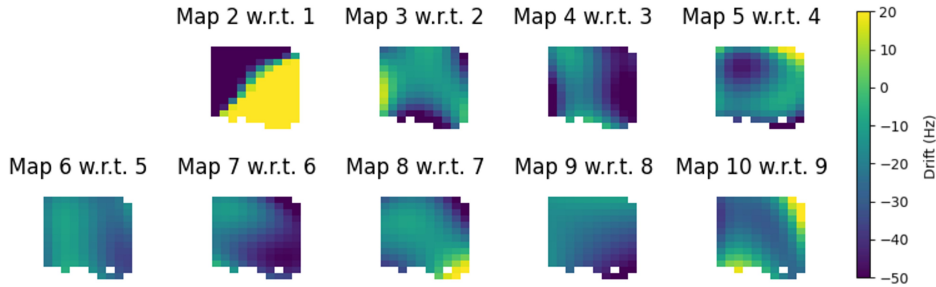


Figure 23: Measurement results for TSE imaging. Drift maps for measurement 12, computed as the difference between subsequent maps. For acquisition parameters, see Table 1.

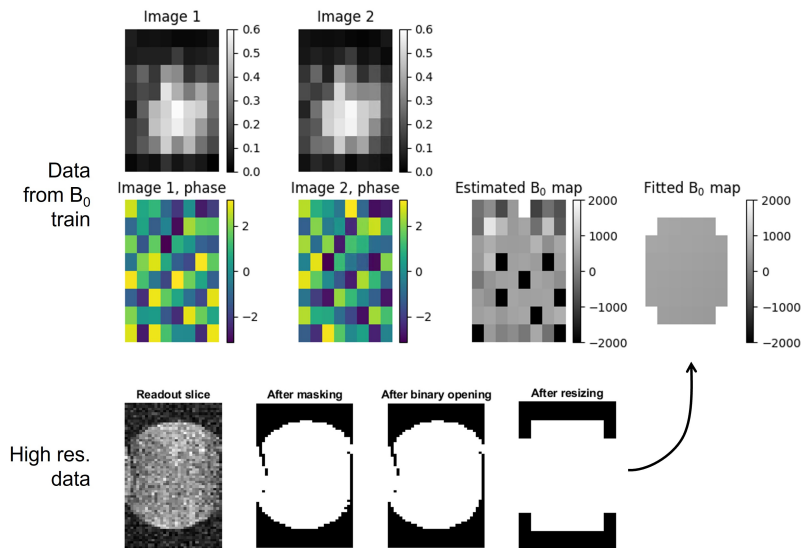
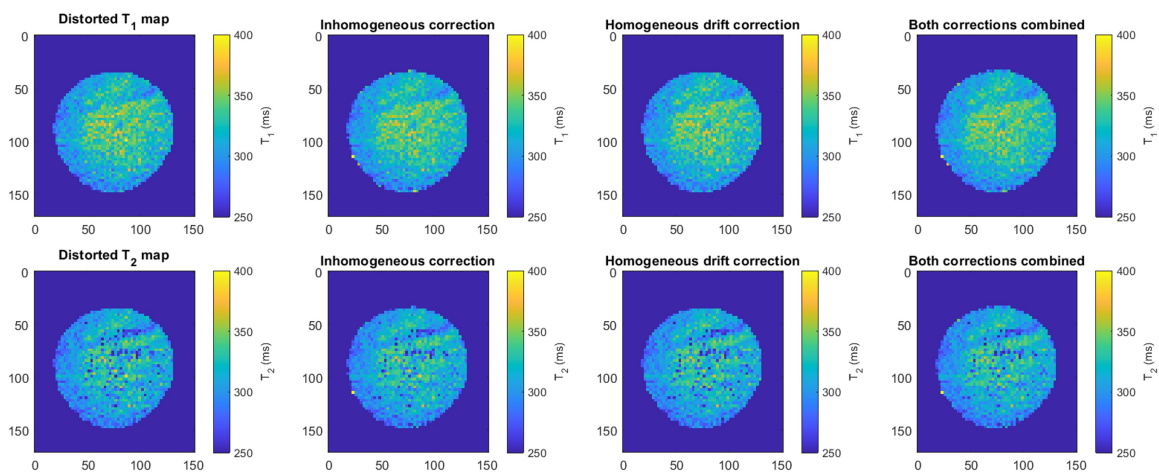
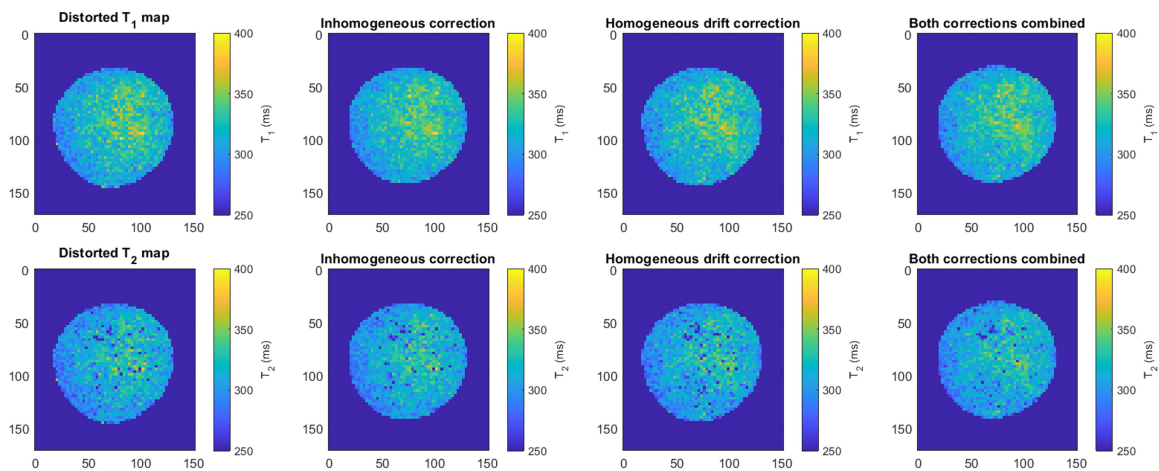


Figure 24: Illustrating the working principle of masking at higher resolution with measured MRF data, showing example images, phase maps and estimated and fitted B₀ maps. The fit is a 0th order fit, the mask is the result of masking at higher resolution.

a) Ball, non-heated



b) Ball, heated



c) Hyperfine phantom, heated

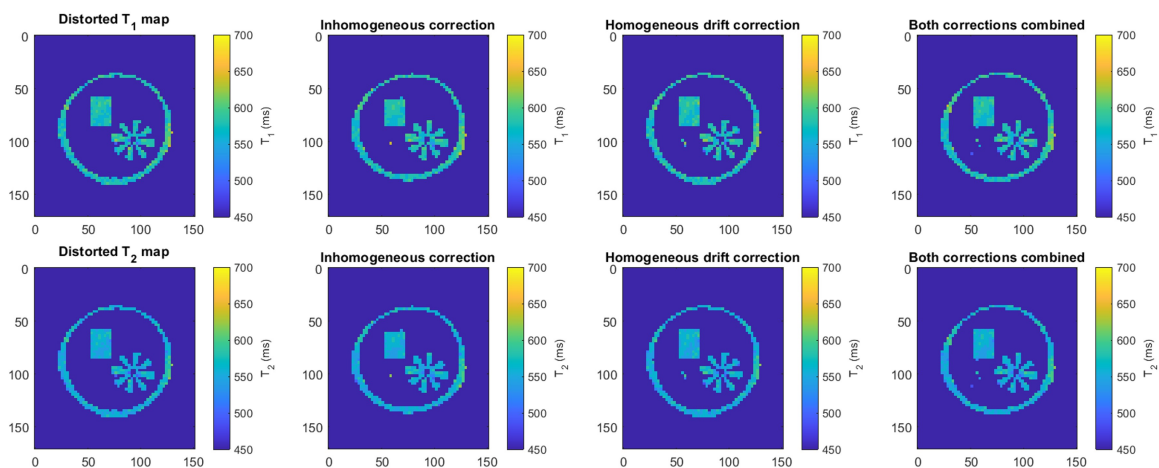


Figure 25: MRF measurement results. Showing a comparison between the distorted and corrected T_1 and T_2 maps for a ball-shaped phantom a) without heating; b) with heating and c) the Hyperfine phantom with heating. 26

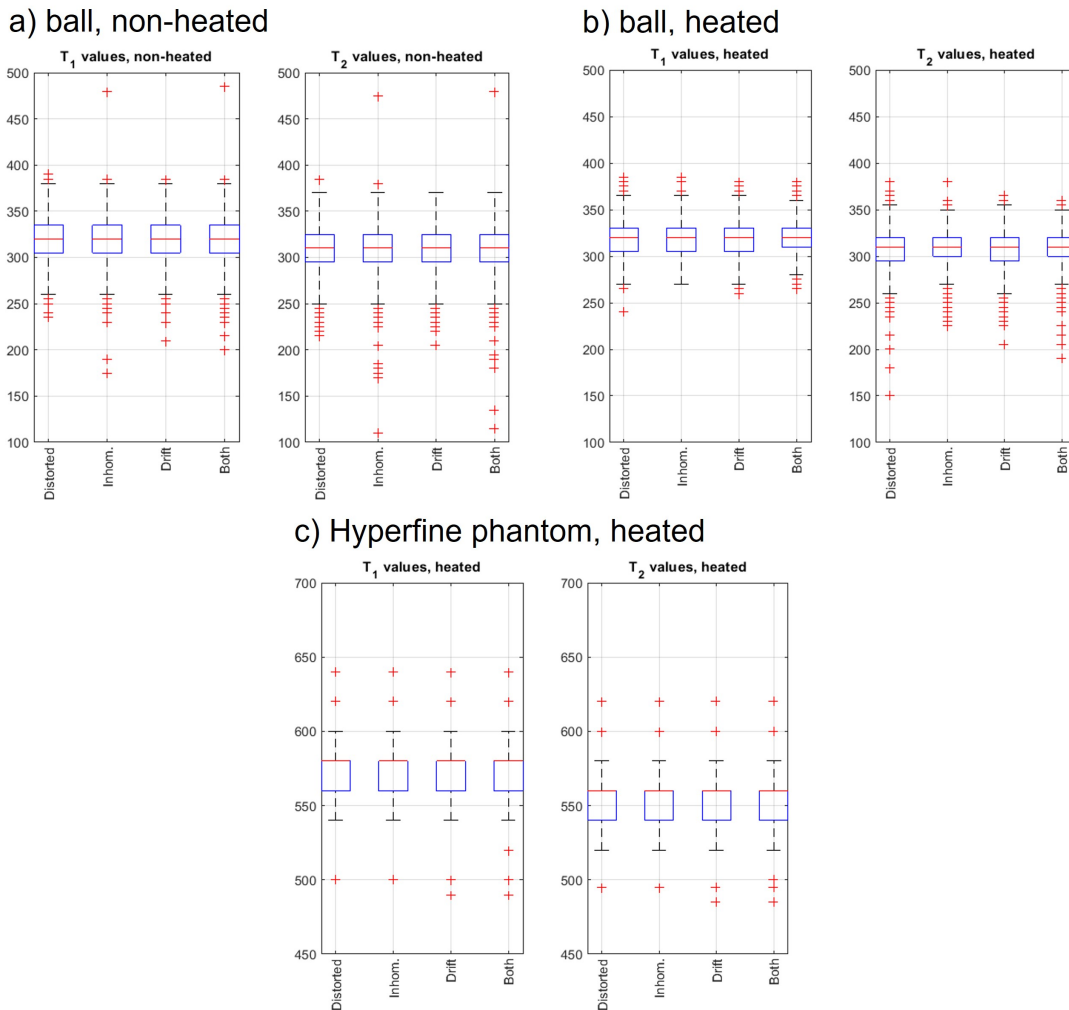


Figure 26: Showing boxplots of the T_1 and T_2 values for the distorted and corrected images for the three measurements. The corresponding maps are shown in Figure 25.

- Ball, heated: center frequency before scanning 2.14880 MHz, after scanning 2.14821 MHz, which implies a frequency drift of 590 Hz. Scan duration 31.5 minutes.
- Hyperfine phantom, heated: center frequency before scanning 2.14865 MHz, after scanning 2.14838 MHz, which implies a frequency drift of 270 Hz. Scan duration of 13.8 minutes.

Although again, like in TSE, the time-dependence of B_0 does not appear to influence the result a lot, the distortion in the images for both corrections combined seem to be less, especially in the case of the heated measurement. In Figure 26, boxplots with T_1 and T_2 values are shown for the distorted and corrected images for all experiments. The T_1 values in all cases for the non-heated and heated ball phantom are 320 ms, the T_2 values 310 ms. The T_1 values in all cases for the Hyperfine phantom are 580 ms, the T_2 values 560 ms.

5 Discussion

In this chapter, the results shown in the previous chapter will be discussed in more detail, starting with TSE and continuing with MRF. Also, some of the implications of these results will be mentioned, and ideas for further research will be proposed.

5.1 Simulation

In the simulation images, it was visible that indeed a homogeneous B_0 leads to an image shift, an inhomogeneous B_0 leads to distortions, and an inhomogeneous and time-dependent B_0 leads to distortions and also appears to introduce additional blurring.

Furthermore, it was visible that the proposed correction method works well. The correction was not perfect, which could be caused by CPR being an approximation. More likely however is the explanation that this is because of the non-integer pixel shifts, as it was observed that the 'rippling' in the image became less when running the simulation at a higher resolution. Ideally, the simulations would have been run at a higher resolution than at the current 30x30 grid, but that was computationally infeasible with the current implementation. A more efficient coding of the simulations or a computer with a larger memory could solve this problem in the future.

In the boxplot in Figure 13, the improvement on the T_1 and T_2 maps is quantified, showing that the error in the matched parameter maps decreases when correcting for distortion. The main reason for this is that there are less outliers, and less signal spreading through multiple regions. This is for example visible in the T_1 values of GM, which surrounds the CSF. In the distorted images (type 2 and 3), there are more high outliers than low outliers, as the signal belonging to the high- T_1 CSF start to leak into the WM region.

It should be noted that the simulations were done without undersampling the signal. This might result in an exaggerated B_0 -effect over time. On the other hand, it ensures that only artefacts resulting from B_0 distortion are visible, by excluding the undersampling artefacts.

5.2 Optimizing B_0 mapping parameters

Figure 14 shows that the drift is quite smooth, suggesting that it is not necessary to collect many B_0 maps. Also, the comparison between 16x16 and 8x8 shows that the general B_0 map layout is also captured in the low resolution map, though some detail is lost. It should be noted that this will only work when a large part of the FOV is filled with signal, otherwise the B_0 map will be based on just a few points. Figure 15 is inconclusive. While a longer TR was expected to reduce the noise-like behaviour of the fitted values, it looks more unstable than the measurement performed with a short TR. In the apple measurement, the drift values in both measurements seems noisy, even after SH fitting. There might be a small effect here, as the drift plot for the long TR shows the drift over a longer period of time than for the short TR.

There is some effect of an increase in TR visible in the first map, which is taken at the beginning of the scan since it looks slightly different than the other maps in short TR measurements. In the measurements with a long TR, or with dummy trains, this is not the case. This is likely caused by the signal not having reached steady state yet at the beginning of the measurement, thus resulting in a slightly different B_0 map. As this might influence the correction result, it is therefore useful to take either $TR \geq 3T_1$ ($TR = 2s$ in Figure 15, for a phantom with $T_1 = 670$ ms, is a factor of $3T_1$). Better still is to use dummy trains, since these have a smaller impact on the acquisition time. The number of dummy trains required was not studied, but the results suggest that 5 dummy trains should suffice.

It is clear from Figure 16 that a longer readout shift improves the stability of the B_0 measurement by increasing the phase difference with respect to the noise level, thus decreasing the error in B_0 estimation. This suggests that it is beneficial to choose a longer t_{shift} over a shorter one. However, a longer t_{shift} will also decrease the signal amplitude and thus affect the signal-to-noise ratio. Therefore it should not be too long.

The fact that all voxels in the low t_{shift} show the same behaviour suggests that there is definitely a trend present in the signal. The source of this trend is unknown.

From these experiments, it is concluded that B_0 mapping in TSE benefits mainly from a longer readout shift. Additionally, B_0 mapping at a very low resolution is possible.

5.3 Distortion correction in TSE

Although it is visible in Figure 17 that B_0 correction does reduce the distortions, the difference between correction with the mean of the B_0 field and using the individual maps appears minimal, see Figure 19. In Figure 21 however, clear differences are visible. A possible explanation for this is the size of the phantom: the ball is one homogeneous phantom, whereas the Hyperfine phantom consists of multiple smaller compartments, so that the ringing might not be visible in the Hyperfine phantom.

It should also be noted here that with these phantoms, small effects at the boundaries of tissues might not be visible, as the phantoms are made of one material. It might be that the correction based on individual B_0 maps would have better results in an in-vivo setting, where multiple different tissues are present. Unfortunately, in-vivo scanning was not possible at the time of the project, further measurements should provide more clarity on this matter.

One other aspect that has to be taken into account while comparing the methods, is the bandwidth per voxel in the image compared to the observed drift. These are, given the bandwidth of 20 kHz in the readout direction:

- Figure 19, measurement 1: Readout 200 Hz/voxel, PE1 400 Hz/voxel, PE2 800 Hz/voxel. Measured drift in the center of the image around 70 Hz.
- Figure 20, measurement 12: Readout 200 Hz/voxel, PE1 200 Hz/voxel, PE2 400 Hz/voxel. Measured drift in the center of the image around 200 Hz.
- Figure 21, measurement 11: 167 Hz/voxel isotropic. Measured drift in the center of the image around 270 Hz.

The lower bandwidths in these two high-resolution scans (measurement 12 and 11) combined with the higher drift values might explain why the correction is more effective, see the highlighted areas in Figures 20 and 21.

As visible in Figure 22, mistakes in the estimation of the B_0 map can introduce artefacts. In this project a 2D spherical harmonic fit was used, each time fitting B_0 for a readout slice. This causes the irregularities visible in the B_0 maps in the left side of the Figure. The B_0 estimation would be more precise and continuous in all dimensions if 3D fitting was applied, especially in places where a readout slice would contain little signal. Another factor that could have influenced the results, especially in Figure 22, are gradient non-linearities caused by imperfect shimming. Near the end of the experiments (measurements 2 and 3), it was observed that due to the heating in the scanner, the shims were off. Thus, even after correction for spatial and temporal B_0 inhomogeneities, some distortion may remain. To find out whether this really is the case, the time-dependent B_0 inhomogeneity correction could be combined with gradient non-linearity correction.

5.4 Distortion correction in MRF

Part of the measurements, including the ball phantom visible in Figure 25, was done with the incorrect pulse length, thus reducing every flip angle by a factor of two. This results in less signal and sub-optimal imaging. However, this data could still be used when using an adapted dictionary for the matching step.

The images resulting from the B_0 trains do not look much like the higher resolution pictures, see Figure 24, which should look like a ball. This is the result of every voxel signal coming from a different flip angle. An additional effect that could decrease voxel signal comes from the large voxel size in a low-resolution image. As the voxel contains spins precessing with different frequencies, some of the signal will cancel out due to intra-voxel dephasing, leading to a lower signal intensity. However, the

masking based on the high resolution image appears to be successful, leading to a correct mask to use for B_0 map estimation.

Another effect that needed to be taken into account during B_0 map acquisition is the multiple phase wraps visible in Figure 24. This leads to imperfect phase unwrapping, thus introducing high outliers in the B_0 map. If a voxel from one echo time has a phase close to π , but from the other echo time close to $-\pi$ due to phase wraps, the B_0 value resulting from the difference in phase will not be representative. Luckily, these are quite recognizable in the image due to their high value and thus easy to filter out.

A comparison between the different methods to correct the MRF images, as seen in Figure 25 shows that when only correcting for inhomogeneity or for drift, some distortion remains. The result for the method in which the two types of distortion corrections are combined seems less distorted.

The ball-shaped phantom has a T_1 and T_2 of 358 ms. For the ball-shaped phantom, average matched T_1 values were 320 ms. For T_2 , the matched values were 310 ms. T_1 and T_2 for the Hyperfine phantom are 670 ms, matched values were 580ms for T_1 and 560 ms for T_2 . For both experiments, matched T_1 and T_2 values were lower than measured. This may have many different reasons, including a slightly different power optimization, B_0 field or temperature, and the use of a different technique to measure the T_1 and T_2 values.

As to T_1 and T_2 values for the ball-shaped phantom, as seen in Figure 26, correction does not really influence those. This suggests that these variations in quantitative values are a result of the MRF sequence and not of B_0 inhomogeneities. However, in the case of a phantom with different tissues, the distortion correction might reduce the errors in dictionary matching, see also the simulation resulting in Figure 13. Therefore, it is recommended that measurements on such a phantom, or in an in-vivo setting, are done in order to investigate this further.

For further research, it is also suggested to analyse distortions both in TSE and in MRF in a quantitative way.

5.5 Minimizing additional scan time

In order to maximize image quality while minimizing additional scan time, several factors have to be taken into account. First of all, it depends on the expected B_0 drift. When the drift appears to be more or less linear, a B_0 map at the beginning and at the end will suffice. However, when this is not the case, more maps need to be measured. In vivo, the drift is expected to be comparable to the simulated heating experiments, though it is likely that outside lab conditions, inhomogeneities are larger and drift values are higher.

Also, the B_0 map size is an important factor, as the additional scanning time scales with the number of voxels in the B_0 map. It should also be noted that the acquisition of a B_0 map might take relatively longer in TSE compared to MRF, depending on TSE parameters like the ETL and the B_0 map size, as in MRF it can be done in one train.

As visible in Table 1, the additional scan time can amount to over 100%, which will lead to increased motion artefacts and decreased patient comfort. Therefore, it is important for future study to find ways in which to minimize additional scan time.

Further research can be done into integrating the B_0 estimation in the imaging acquisition, as part of the data is sampled double in the interleaved sequences. Also, it would be interesting to explore other ways to make the B_0 map estimation less time-consuming, such as undersampling, increasing the ETL for B_0 mapping only, using a part of the image acquisition data.

6 Conclusion

Dynamic B_0 correction in TSE may be a successful method to correct for time-dependent and inhomogeneous B_0 fields at low field strengths. Measurements done show that the method works, though the time-dependent drift was not strong enough to show benefits over a correction with only one B_0 map. Despite this, the method might still be useful to apply this in cases where frequency drifts are very strong or very inhomogeneous. Another application would be when the image needs to be acquired at higher resolution. These images have a smaller bandwidth per voxel and are thus more sensitive to the shift induced by drift. Also, the acquisition of these images generally takes longer, so the actual drift is higher. Further measurements should provide more clarity on this subject.

In MRF, time-dependent and inhomogeneous B_0 correction would result in a very long reconstruction time. Therefore three other methods have been compared: correcting for average inhomogeneity, correcting for time-dependent drift, and correcting for both. The correction for inhomogeneity yields good results, but the distortion appears to decrease even further when combining this with a homogeneous and time-dependent drift correction, where this drift is estimated from the interleaved B_0 mapping trains. The correction does not appear to influence the T_1 and T_2 values in the homogeneous phantoms, though the simulation results suggest that in a tissue-like phantom, distortion correction will result in a better estimation of the quantitative parameter maps.

7 Acknowledgements

Many people have helped me during my thesis, for which I am very grateful. I would like to thank the members of the Low Field group of the Gorter Center at the LUMC, and especially Tom O'Reilly, for their ideas and help during the measurements. I am also thankful for the supervision of Kirsten Koolstra (LUMC), who as my daily supervisor helped me through the ups and downs of this project. I thank Frans Vos, my TU Delft-supervisor, his insights helped me to look critically at my own work.

References

- [1] WHO, “Total density per million population: Magnetic resonance imaging (world health organization),” 2022. [Online]. Available: <https://www.who.int/data/gho/data/indicators/indicator-details/GHO/total-density-per-million-population-magnetic-resonance-imaging>.
- [2] OECD, “Magnetic resonance imaging (mri) units,” 2018. DOI: <https://doi.org/https://doi.org/10.1787/1a72e7d1-en>. [Online]. Available: <https://www.oecd-ilibrary.org/content/data/1a72e7d1-en>.
- [3] J. P. Marques, F. F. Simonis, and A. G. Webb, “Low-field mri: An mr physics perspective,” *Journal of magnetic resonance imaging*, vol. 49, no. 6, pp. 1528–1542, 2019.
- [4] T. O’Reilly, W. M. Teeuwisse, D. de Gans, K. Koolstra, and A. G. Webb, “In vivo 3d brain and extremity mri at 50 mt using a permanent magnet halbach array,” *Magnetic resonance in medicine*, vol. 85, no. 1, pp. 495–505, 2021.
- [5] J. Obungoloch, J. R. Harper, S. Consevage, *et al.*, “Design of a sustainable prepolarizing magnetic resonance imaging system for infant hydrocephalus,” *Magnetic Resonance Materials in Physics, Biology and Medicine*, vol. 31, no. 5, pp. 665–676, 2018.
- [6] K. Koolstra, T. O’Reilly, P. Börnert, and A. Webb, “Image distortion correction for mri in low field permanent magnet systems with strong b_0 inhomogeneity and gradient field nonlinearities,” *Magnetic Resonance Materials in Physics, Biology and Medicine*, pp. 1–12, 2021.
- [7] M. Sagawa, S. Hirose, H. Yamamoto, S. Fujimura, and Y. Matsuura, “Nd-Fe-B permanent magnet materials,” *Japanese journal of applied physics*, vol. 26, no. 6R, p. 785, 1987.
- [8] C. Z. Cooley, J. P. Stockmann, B. D. Armstrong, *et al.*, “Two-dimensional imaging in a lightweight portable mri scanner without gradient coils,” *Magnetic resonance in medicine*, vol. 73, no. 2, pp. 872–883, 2015.
- [9] R. W. Brown, Y.-C. N. Cheng, E. M. Haacke, M. R. Thompson, and R. Venkatesan, *Magnetic resonance imaging: physical principles and sequence design*. John Wiley & Sons, 2014.
- [10] M. Usman, L. Kakkar, A. Matakos, A. Kirkham, S. Arridge, and D. Atkinson, “Joint b_0 and image estimation integrated with model based reconstruction for field map update and distortion correction in prostate diffusion mri,” *Magnetic resonance imaging*, vol. 65, pp. 90–99, 2020.
- [11] M. L. de Leeuw den Bouter, M. B. van Gijzen, and R. F. Remis, “Conjugate gradient variants for p-regularized image reconstruction in low-field mri,” *SN Applied Sciences*, vol. 1, no. 12, pp. 1–15, 2019.
- [12] L.-C. Man, J. M. Pauly, and A. Macovski, “Multifrequency interpolation for fast off-resonance correction,” *Magnetic resonance in medicine*, vol. 37, no. 5, pp. 785–792, 1997.
- [13] H. E. Nijssse, “Temperature field drift monitoring in low-field mr.”
- [14] D. W. McRobbie, E. A. Moore, M. J. Graves, and M. R. Prince, *MRI from Picture to Proton*. Cambridge university press, 2017.
- [15] D. Ma, V. Gulani, N. Seiberlich, *et al.*, “Magnetic resonance fingerprinting,” *Nature*, vol. 495, no. 7440, pp. 187–192, 2013.
- [16] B. Bipin Mehta, S. Coppo, D. Frances McGivney, *et al.*, “Magnetic resonance fingerprinting: A technical review,” *Magnetic resonance in medicine*, vol. 81, no. 1, pp. 25–46, 2019.
- [17] P. Su, D. Mao, P. Liu, *et al.*, “Multiparametric estimation of brain hemodynamics with mr fingerprinting asl,” *Magnetic resonance in medicine*, vol. 78, no. 5, pp. 1812–1823, 2017.
- [18] A. Panda, B. B. Mehta, S. Coppo, *et al.*, “Magnetic resonance fingerprinting—an overview,” *Current opinion in biomedical engineering*, vol. 3, pp. 56–66, 2017.

- [19] K. Koolstra, J.-W. M. Beenakker, P. Koken, A. Webb, and P. Börnert, “Cartesian mr fingerprinting in the eye at 7t using compressed sensing and matrix completion-based reconstructions,” *Magnetic resonance in medicine*, vol. 81, no. 4, pp. 2551–2565, 2019.
- [20] Y. Jiang, D. Ma, N. Seiberlich, V. Gulani, and M. A. Griswold, “Mr fingerprinting using fast imaging with steady state precession (fisp) with spiral readout,” *Magnetic resonance in medicine*, vol. 74, no. 6, pp. 1621–1631, 2015.
- [21] P. Boernert, H. Schomberg, B. Aldefeld, and J. Groen, “Improvements in spiral mr imaging,” *Magnetic Resonance Materials in Physics, Biology and Medicine*, vol. 9, no. 1, pp. 29–41, 1999.
- [22] E. Yudilevich and H. Stark, “Spiral sampling in magnetic resonance imaging—the effect of inhomogeneities,” *IEEE transactions on medical imaging*, vol. 6, no. 4, pp. 337–345, 1987.
- [23] G. Mazor, L. Weizman, A. Tal, and Y. C. Eldar, “Low-rank magnetic resonance fingerprinting,” *Medical physics*, vol. 45, no. 9, pp. 4066–4084, 2018.
- [24] B. Zhao, K. Setsompop, E. Adalsteinsson, *et al.*, “Improved magnetic resonance fingerprinting reconstruction with low-rank and subspace modeling,” *Magnetic resonance in medicine*, vol. 79, no. 2, pp. 933–942, 2018.
- [25] B. Zhao, “Model-based iterative reconstruction for magnetic resonance fingerprinting,” in *2015 IEEE International Conference on Image Processing (ICIP)*, IEEE, 2015, pp. 3392–3396.
- [26] C. Boyer, N. Chauffert, P. Ciuciu, J. Kahn, and P. Weiss, “On the generation of sampling schemes for magnetic resonance imaging,” *SIAM Journal on Imaging Sciences*, vol. 9, no. 4, pp. 2039–2072, 2016.
- [27] K. Koolstra, A. Webb, P. Koken, K. Nehrke, and P. Börnert, “Water-fat separation in spiral magnetic resonance fingerprinting using conjugate phase reconstruction,” in *Proceedings of the 26th Annual Meeting of ISMRM, Paris, France*, 2018, p. 681.
- [28] H. M. Gach, C. Tanase, and F. Boada, “2d & 3d shepp-logan phantom standards for mri,” in *2008 19th International Conference on Systems Engineering*, IEEE, 2008, pp. 521–526.
- [29] T. O’Reilly and A. G. Webb, “In vivo t1 and t2 relaxation time maps of brain tissue, skeletal muscle, and lipid measured in healthy volunteers at 50 mt,” *Magnetic Resonance in Medicine*, vol. 87, no. 2, pp. 884–895, 2022.
- [30] K. Werz, H. Braun, D. Vitha, *et al.*, “Relaxation times t1, t2, and t2* of apples, pears, citrus fruits, and potatoes with a comparison to human tissues,” *Zeitschrift für Medizinische Physik*, vol. 21, no. 3, pp. 206–215, 2011.